



Implicit numerical integration and consistent linearization of inelastic constitutive models of rock salt



Thomas Nagel^{a,b,*}, Wolfgang Minkley^c, Norbert Böttcher^{a,d}, Dmitri Naumov^{e,a}, Uwe-Jens Görke^a, Olaf Kolditz^{a,f}

^a Helmholtz Centre for Environmental Research – UFZ, Leipzig, Germany

^b Trinity College Dublin, Dublin, Ireland

^c Institut für Gebirgsmechanik GmbH, Leipzig, Germany

^d Federal Institute for Geosciences and Natural Resources, Hannover, Germany

^e Leipzig University of Applied Sciences, Leipzig, Germany

^f Technische Universität Dresden, Dresden, Germany

ARTICLE INFO

Article history:

Received 25 July 2016

Accepted 17 November 2016

Available online 19 December 2016

Keywords:

Host rock material
Viscoplastic material
Finite elements
Thermomechanics
Implicit scheme
OpenGeoSys

ABSTRACT

The mechanical behavior of rock salt formations is not only of interest due to mining of salt but also because of its increasing relevance for geotechnical applications, e.g., for the storage of strategic oil and gas reserves, for hosting nuclear waste repositories, for compressed air energy storage (CAES) or the cavern storage of hydrogen. The safety assessment of geotechnical installations as well as long-term convergence predictions of salt caverns require models capturing the inelastic behavior of rock salt under thermomechanical loading. Many models have been derived for uniaxial or triaxial experimental setups and some are inadequately presented to fully describe three-dimensional scenarios. Here, a tensorial representation is chosen to avoid such inconsistencies and their possible consequences on commonly used material parameters are discussed. Two very commonly used material models, the LUBBY2 and Minkley formulations, have been primarily implemented into software relying on explicit time integration schemes. Here, their implicit implementation with analytical Jacobians into a scientific open-source finite element framework is described in detail. The implementations are verified by comparison to suitable analytical solutions for coupled thermomechanical loadings and their convergence behavior is analyzed.

© 2016 Elsevier Ltd. All rights reserved.

1. Introduction

The mechanical behavior of rock salt formations is not only of interest due to mining of salt but also because of the increasing use for geotechnical applications [1]. The tight morphology of rock salt makes it an ideal material for the storage of matter [2,3]. Solution-mined caverns in underground salt domes have been used for the storage of strategic oil and gas reserves for decades. Salt formations are also discussed as candidate formations for hosting nuclear and other waste repositories [4–8]. In the context of the transition to volatile renewable energies, compressed air energy storage (CAES) in salt caverns is discussed to mitigate fluctuations in wind energy for continuous electricity production [9–14]. Finally, the cavern storage of hydrogen as a chemical energy

carrier produced electrolytically from renewable energy sources has gained scientific interest [2].

The safety of salt mines as well as the long-term convergence behavior of salt caverns have been assessed based on thermomechanical models of the inelastic behavior of rock salt [5,14–19]. Rock salt is a material exhibiting several modes of creep and plasticity [20,21]. Different, usually viscoplastic, salt models have been developed in the past by various groups of specialists in order to represent the mechanical characteristics of rock salt under laboratory and field conditions [22–29]. Lately, in the context of the novel applications outlined above, an increased and broader interest into the mechanical behavior of rock salt due to a more intense use of the subsurface for energy storage and conversion has developed. These novel applications also shift the focus of the analyses somewhat from the long-term behavior to short-term phenomena induced on the time scale relevant for renewable energy applications [3,7]. For example, while the time scales of pressure changes in caverns used for strategic oil and gas reserves or seasonal energy

* Corresponding author at: Helmholtz Centre for Environmental Research – UFZ, Leipzig, Germany.

E-mail address: thomas.nagel@ufz.de (T. Nagel).

Nomenclature¹

Greek symbols

α_T	linear thermal expansion coefficient
ϵ, ϵ	small strain tensor/its Kelvin mapping
η	shear viscosity
η_{vol}	bulk viscosity
$d\Gamma$	area element
$d\Omega$	volume element
ψ^i	residual in iteration i
ρ	mass density
σ, σ	cauchy stress tensor/its Kelvin mapping
θ	lode angle

Operators

$\langle \bullet \rangle$	McCauley brackets
$\mathbf{a} \cdot \mathbf{b}$	dot product of \mathbf{a} and \mathbf{b}
$\mathbf{A} : \mathbf{B}$	double contraction of \mathbf{A} and \mathbf{B}
$\mathbf{a} \otimes \mathbf{b}$	dyadic product of \mathbf{a} and \mathbf{b}
$\mathbf{A} \odot \mathbf{B}$	$\frac{1}{2} \left[(\mathbf{A} \otimes \mathbf{B})^T + (\mathbf{A} \otimes \mathbf{B}) \right]$
$\mathbf{A} \ominus \mathbf{B}$	$\frac{1}{2} \left[(\mathbf{A} \otimes \mathbf{B})^T - (\mathbf{A} \otimes \mathbf{B}) \right]$
$\langle \bullet \rangle^D$	deviatoric part of a tensor
div	divergence operator
grad	gradient operator
$\langle \bullet \rangle^S$	spherical part of a tensor

$\langle \bullet \rangle^T, \langle \bullet \rangle^{ab}$ transpose operator; transposition of a th and b th basis vector

Roman symbols

\mathbf{b}	external body force
\mathcal{C}, \mathbf{C}	tangent moduli (fourth order tensor/its Kelvin mapping)
\mathbf{e}_i	Cartesian basis vectors with $\mathbf{e}_i \cdot \mathbf{e}_j = \delta_{ij}$
\mathbf{e}	volume strain
F	yield function
G	shear modulus
G_F	plastic potential
\mathbf{I}	Kelvin representation of an identity tensor
I_1	first principal invariant
J_2	second deviatoric invariant
J_3	third deviatoric invariant
K	bulk modulus
\mathbf{n}	outward unit normal vector
N_a, \mathbf{N}	nodal shape function, element matrix of nodal shape functions
$\mathbf{0}$	Kelvin representation of a zero tensor
$\mathcal{P}^S, \mathcal{P}^D$	spherical and deviatoric projection tensors
$\mathbf{P}^S, \mathbf{P}^D$	spherical and deviatoric projection matrices
p	hydrostatic pressure
\mathbf{t}	surface traction
\mathbf{u}	displacement vector
\mathcal{V}	viscosity tensor

storage concepts are on the order of months and years, caverns of CAES power plants have to withstand significant pressure fluctuations several times a day or week. The increasing use of the subsurface and the evaluation of partially competing usage concepts are the motivation to revisit the existing formulations for the constitutive behavior of rock salt and to incorporate them into continuum mechanical and numerical frameworks of current standard for large-scale simulations.

Among the models listed above, typical constitutive formulations for rock salt include the LUBBY2 model and the model series by Minkley et al., both of which have been used extensively in practical geotechnical settings. The LUBBY2 model [22,30] is a non-linear viscoelastic model based on a Burgers-type rheological analogue. Minkley [26] extended this setup by an additional friction element of a modified Mohr-Coulomb type to capture plasticity with strain hardening and softening as well as dilatancy. These effects allow a characterization of, e.g., excavation damaged zones (EDZ) around geotechnical installations. The plastic submodel includes the dependence of the yield surface and the plastic potential on the stress state and on the deformation history, e.g. [28]. Wang et al. [31] used a similar model but employed a Drucker-Prager yield surface with tension cut-off as well as a WIPP creep model, see also [21]. Large displacements and rotations have been taken into account in Ref. [32]. Some studies have investigated hydro-mechanical couplings that become important in the near- and far-field of geotechnical installations when dilatancy or damage open up flow paths in the rock salt that is otherwise considered tight [1–3,33,34]; see also [35,36] for recent works on hydromechanical coupling in a geotechnical context.

Many rock salt models have been derived for uniaxial or triaxial experimental setups and have only later on been generalized to

three dimensions in a post hoc manner which is not always appropriate to fully describe three-dimensional scenarios [15,16,22]. Here, a tensorial representation is chosen, overcoming these inconsistencies. We further highlight the different treatment of material parameters existing in the literature due to the mix of uniaxial and three-dimensional formulations.

Specifically for large-scale geotechnical studies, the numerical implementation of the existing rock salt models has hardly been discussed in detail. Most of the known formulations have been implemented into software relying on explicit time integration schemes which are not unconditionally stable [24,28,29,31,32]. An implicit time integration based on a generalized mid-point rule has been employed by Pudewills and Krauss [37] whereas a Crank-Nicholson time integration scheme has been used in [23]. However, none of these studies provide details on the constitutive tangent matrices nor illustrate the convergence behavior of the implemented algorithms. Here, a state-of-the-art implicit implementation of the LUBBY2 and Minkley models into the scientific open-source parallelized finite element framework OpenGeoSys [38] is described in detail, compare for example the Refs. [39–52] regarding implicit finite element implementations. This will form the basis for large scale simulations in the context of competing usage concepts of the subsurface [53].

The outline of the article is as follows: in Section 2, the general numerical framework of the finite element code used in this study is presented. Section 3 clarifies some general aspects of the Burgers model that forms the basis of several constitutive models of rock salt. These considerations are specified for the LUBBY2 model in Section 4. A general tensorial formulation of this model is introduced and compared to the classical version prevalent in literature. In Section 5, the Burgers model is extended by a friction element without considering any specific yield surface or plastic potential to provide the implementation of a generalized viscoplastic model. Plastic flow regularization in the case of softening materials is pro-

¹ Throughout the article bold face symbols denote tensors and vectors. Normal face letters represent scalar quantities.

vided by a simple Perzyna approach [54,55]. The Mohr-Coulomb yield surface used in modified form in the original formulation of the Minkley model [26] is re-cast into an invariant formulation in Section 6 and integrated into the general model presented in Section 5. The implementation of the LUBBY2 and Minkley models is validated against analytical solutions in Section 7 considering coupled thermomechanical loadings. Finally, the convergence behavior of both models is analysed in Section 8 along with some example simulations. The paper closes with a short discussion and conclusions, Section 9.

2. Numerical framework

Both the equilibrium iteration of the global displacement-based formulation of the solid momentum balance as well as the local stress update procedures are based on a consistent linearization in the context of a Newton-Raphson procedure. This approach is known to lead to an efficient coupling of both implementation levels [45].

2.1. Equilibrium iteration

The local form of the quasistatic equilibrium conditions derived from the momentum balance reads

$$\text{div } \boldsymbol{\sigma} + \boldsymbol{q} \mathbf{b} = \mathbf{0} \quad (1)$$

and is the basis to determine the displacement field \mathbf{u} in a domain Ω . A test function \mathbf{v} is chosen that is kinematically compatible and satisfies $\mathbf{v} = \mathbf{0} \forall \mathbf{x} \in \partial\Omega_u$ with $\mathbf{u} = \bar{\mathbf{u}} \forall \mathbf{x} \in \partial\Omega_u$, i.e. it vanishes on the Dirichlet boundary $\partial\Omega_u$. Multiplication of Eq. (1) with the test function and integration over the domain Ω leads to the weak form of the equilibrium conditions

$$\int_{\Omega} \boldsymbol{\sigma} : \text{grad } \mathbf{v} \, d\Omega = \int_{\partial\Omega_t} \bar{\mathbf{t}} \cdot \mathbf{v} \, d\Gamma - \int_{\Omega} \boldsymbol{q} \mathbf{b} \cdot \mathbf{v} \, d\Omega \quad (2)$$

with the prescribed surface traction vector $\bar{\mathbf{t}}$ on the Neumann boundary $\partial\Omega_t$ occurring naturally after partial integration. In seeking stresses and strains of the next load step designated by $t + \Delta t$, a linearization is performed around the current state given by the i th global Newton-Raphson iteration

$$\begin{aligned} \int_{\Omega} \text{grad } \mathbf{v} : \frac{d\boldsymbol{\sigma}}{d\boldsymbol{\epsilon}} \Big|_i : \Delta \boldsymbol{\epsilon}^{i+1} \, d\Omega &= \int_{\partial\Omega_t} \bar{\mathbf{t}}^{t+\Delta t} \cdot \mathbf{v} \, d\Gamma - \int_{\Omega} \boldsymbol{q} \mathbf{b}^{t+\Delta t} \cdot \mathbf{v} \, d\Omega \\ &- \int_{\Omega} \boldsymbol{\sigma}^i : \text{grad } \mathbf{v} \, d\Omega \end{aligned} \quad (3)$$

where infinitesimal deformations and conservative loads have been assumed. Eq. (3) introduces the constitutive tangent modulus

$$\mathcal{C} = \frac{d\boldsymbol{\sigma}}{d\boldsymbol{\epsilon}} \quad (4)$$

2.2. Kelvin mapping for the finite element implementation

Commonly, the transition to a standard matrix-vector notation in the context of finite element implementations is performed by replacing three-dimensional symmetric second order tensors by six-dimensional vectors (using engineering shear strains $\gamma_{ij} = 2\epsilon_{ij}$) and three-dimensional fourth order tensors by 6×6 matrices. This *Voigt mapping* leads to a different treatment of, e.g., stresses and strains and does not preserve tensor norms. Here, the *Kelvin mapping* will be preferred which introduces a new 6D basis $\{\mathbf{E}_I\}$ such that the tensor character of all quantities is preserved. Thus, exemplary tensors with the necessary symmetries (minor symmetries in the case of the fourth order tensor) can equivalently be written as

$$\mathbf{A} = A_{ij} \mathbf{e}_i \otimes \mathbf{e}_j = A_I \mathbf{E}_I \quad \text{and} \quad \mathcal{A} = A_{ijkl} \mathbf{e}_i \otimes \mathbf{e}_j \otimes \mathbf{e}_k \otimes \mathbf{e}_l = A_{IJ} \mathbf{E}_I \otimes \mathbf{E}_J \quad (5)$$

For details on the finite element implementation of the Kelvin mapping and its advantages we refer the reader to [56] and the references cited therein.

In the sequel, a switch to a matrix-vector notation representative of the finite element implementation will be highlighted by italic bold-face symbols. The matrix and vector entries correspond to the coordinate matrices obtained by the Kelvin mapping.

The domain of interest is split into standard finite elements characterized by a set of nodal shape functions $N_a(\mathbf{x})$. The sought solution vector \mathbf{u} in a point is approximated by

$$\mathbf{u} \approx \tilde{\mathbf{u}} = \sum_a^{n_{\text{nodes}}} N_a \hat{\mathbf{u}}_a = \mathbf{N} \hat{\mathbf{u}} \quad (6)$$

where $\hat{\mathbf{u}}$ is the nodal displacement vector of the element containing the point at which \mathbf{u} is evaluated, \mathbf{N} is the element matrix of shape functions and n_{nodes} is the number of nodes of said element. In the isoparametric concept employed here, the position vector \mathbf{x} and the test function \mathbf{v} are approximated likewise. Similarly, the \mathbf{B} matrix containing the gradients of the shape functions can be introduced to enable the calculation of strain vectors from the nodal displacements (for details see, e.g., [45]):

$$\boldsymbol{\epsilon} = \text{symgrad } \mathbf{u} = \mathbf{B} \hat{\mathbf{u}} \quad \text{and} \quad \text{symgrad } \mathbf{v} = \mathbf{B} \hat{\mathbf{v}} \quad (7)$$

Substitution of these relations into Eq. (3) allows the elimination of the arbitrary nodal values $\hat{\mathbf{v}}$ of the test functions and produces the equation system for each elemental domain Ω^e :

$$\begin{aligned} \int_{\Omega^e} \mathbf{B}^T \mathcal{C}^i \mathbf{B} \, d\Omega \, \Delta \hat{\mathbf{u}}^{i+1} &= \int_{\partial\Omega_t^e} \mathbf{N}^T \bar{\mathbf{t}}^{t+\Delta t} \, d\Gamma - \int_{\Omega^e} \mathbf{N}^T \boldsymbol{q} \mathbf{b}^{t+\Delta t} \, d\Omega \\ &- \int_{\Omega^e} \mathbf{B}^T \boldsymbol{\sigma}^i \, d\Omega \end{aligned} \quad (8)$$

The integral on the left hand side defines the stiffness matrix \mathbf{K} , the right-hand side defines the residual vector $\boldsymbol{\psi}$ such that the linearized system reads

$$\mathbf{K}^i \Delta \hat{\mathbf{u}}^{i+1} = \boldsymbol{\psi}^i \quad (9)$$

The contributions of all elements are assembled into the global problem which is then solved for the vector of unknown displacement increments $\Delta \hat{\mathbf{u}}^{i+1}$.

In summary, a constitutive equation for the stresses is required to correctly calculate the residual vector $\boldsymbol{\psi}^i$ on the right-hand side of Eq. (8) as well as the (usually solution dependent) \mathcal{C}^i -matrix containing the material moduli in an algorithmically consistent manner [46].

2.3. Stress integration

The equations necessary for the integration of the stress increments usually lead to a differential-algebraic equation system [57] of the form

$$\mathbf{0} = \mathbf{r}(\mathbf{z}, \boldsymbol{\epsilon}^i) \quad (10)$$

where \mathbf{r} represents the residual vector describing the evolution equations for stresses and internal variables, as well as constraints (e.g. the consistency condition in elasto-plasticity). Note, that in the local iterations to solve the above equation system, $\boldsymbol{\epsilon}^i$ from the global iteration is considered fixed. The state vector \mathbf{z} contains the stress vector as well as the constitutive model's internal state variables ($\boldsymbol{\kappa}_k, \kappa_k$):

$$\mathbf{z} = (\boldsymbol{\sigma}^T, \boldsymbol{\kappa}_k^T, \kappa_k)^T \quad (11)$$

The evolution equations most often involve rates in the form of first order time derivatives. Considering the general ordinary differential equation

$$\dot{y} = f(y), \quad (12)$$

time discretization of the rate quantities in the functionals is based here on a generalized single step scheme. We write for a time step in the interval $[t, t + \Delta t]$

$$y^{t+\Delta t} = y^t + \Delta t [\alpha f^{t+\Delta t} + (1 - \alpha)f^t] \quad (13)$$

which includes the schemes

$$\alpha = \begin{cases} 0 & \text{Euler forward (explicit)} \\ 0.5 & \text{Crank-Nicolson} \\ 1 & \text{Euler backward (implicit)} \end{cases} \quad (14)$$

With this relationship, a rate of change at time $t + \Delta t$ can be approximated based solely on known quantities and the unknown primary variable at time $t + \Delta t$:

$$\dot{y}^{t+\Delta t} = \frac{y^{t+\Delta t} - y^t}{\alpha \Delta t} - \frac{y^t}{\alpha \Delta t} - \frac{1 - \alpha}{\alpha} f^t \quad (15)$$

Note, that for $\alpha = 0$, the above relationship cannot be used directly but the rate at time t is used directly and exclusively. A Taylor series expansion of the differential-algebraic system yields the iteration procedure for the local stress integration

$$-r^j = \frac{\partial r}{\partial z_j} \Delta z^{j+1} \quad (16)$$

Once the iteration has converged, we find the consistent tangent matrix for the global iteration using the total differential of r and the fact that the first entry in z is always σ :

$$\frac{dr}{d\epsilon^{t+\Delta t}} = \frac{\partial r}{\partial \epsilon^{t+\Delta t}} + \left(\frac{\partial r}{\partial z} \right)_{t+\Delta t} \frac{dz}{d\epsilon^{t+\Delta t}} = 0 \quad (17)$$

The first entry of the solution $dz/d\epsilon^{t+\Delta t}$ to the resulting linear system

$$\left(\frac{\partial r}{\partial z} \right)_{t+\Delta t} \frac{dz}{d\epsilon^{t+\Delta t}} = - \frac{\partial r}{\partial \epsilon^{t+\Delta t}} \quad (18)$$

is the sought tangent matrix C^t . Thus, the tangent modulus matrix can be computed with very little extra effort based on the already known Jacobian from the local stress-update procedure and is automatically consistent with the integration algorithm chosen. The latter point is of importance for achieving the best possible convergence of the global problem [45,46].

2.4. Coupling to thermal fields

When considering applications such as nuclear waste storage and CAES, thermal fields influence the material behavior of the rock salt by lowering elastic moduli and viscosity parameters or by increasing healing rates. For a general thermomechanical coupling, a monolithic scheme is conceivable where the coupling matrices result from the dependence of one PDE on the primary variable of the other:

$$\begin{pmatrix} K_{uu} & K_{uT} \\ K_{Tu} & K_{TT} \end{pmatrix} \begin{pmatrix} \Delta u \\ \Delta T \end{pmatrix} = \begin{pmatrix} \psi_u \\ \psi_T \end{pmatrix} \quad (19)$$

In general, mechanical work can be partially dissipated into heat and thus lead to local temperature changes. However, for the strain rates relevant here, the coupling to temperature fields can be described as uni-directional, i.e. the temperature distribution affects the mechanical problem but not the other way around. Therefore, an efficient solution technique is to couple the thermal

and mechanical initial boundary value problems (IBVP) in a staggered/partitioned fashion. In other words, with ϱc_p the volumetric isobaric heat capacity and λ the thermal conductivity tensor, the PDE-system

$$\text{PDE 1 : } 0 = \varrho c_p \frac{\partial T}{\partial t} - \text{div}(\lambda \text{grad} T) \quad (20)$$

$$\text{PDE 2 : } 0 = \text{div}(\sigma(u, T)) - \varrho b = 0 \quad (21)$$

is addressed by an algorithm which solves the PDE governing one of the primary variables (temperature and displacement) while keeping the other fixed and iterating until convergence. Choosing an FE residual formulation this may be illustrated by

$$K_{TT} \Delta T = \psi_T - f(u) \quad \text{with } u \text{ fixed} \quad \leftrightarrow \quad K_{uu} \Delta u = \psi_u - f(T) \quad \text{with } T \text{ fixed} \quad (22)$$

where the residuals may be modified by source term-like contributions from the other coupled processes. In case of the one way coupling considered here, i.e. $K_{Tu} = 0$, the thermal IBVP is solved first, followed by the solution of the mechanical IBVP without any further iteration between both processes being necessary. Details on weak forms of coupled problems and possible implementations can be found in standard references, e.g. [58].

The inclusion of temperature-dependent material parameters and thermal strains is an inherent part of the algorithm described below and will be illustrated by suitable tests. For that purpose, the strain tensor ϵ and the volume strain e refer to the mechanical part of the deformation, in other words in all subsequent equations

$$\epsilon = \epsilon_{\text{tot}} - \epsilon_{\text{th}} = \epsilon_{\text{tot}} - \alpha_T \Delta T \mathbf{I} \quad \text{and} \quad e = e_{\text{tot}} - e_{\text{th}} = e_{\text{tot}} - 3\alpha_T \Delta T \quad (23)$$

is inferred. The temperature dependence of certain parameters will not be made explicit in the notation. Please also refer to [22,40,59–61].

3. A generalised Burgers model

Many models of salt mechanics are based on a rheological model of the Burgers type in order to represent primary and secondary (stationary) creep. A generalized version is introduced that does not require certain assumptions typically associated with this model type in salt mechanics, such as isotropy.

The Burgers model comprises a Maxwell element in series with a Kelvin element (Fig. 1). This model is described by the following set of evolution equations

$$\sigma = C_M : [\epsilon - \epsilon_K - \epsilon_M] \quad (24)$$

$$\dot{\epsilon}_K = \mathcal{V}_K^{-1} : (\sigma - C_K : \epsilon_K) \quad (25)$$

$$\dot{\epsilon}_M = \mathcal{V}_M^{-1} : \sigma \quad (26)$$

where the strain in the Kelvin element as well as the strain in the dashpot of the Maxwell element represent internal variables. The Kelvin element describes transient (primary) creep, while the Maxwell element describes stationary (secondary) creep. For physical reasons, the viscosity tensor \mathcal{V}_M needs to be constructed such that

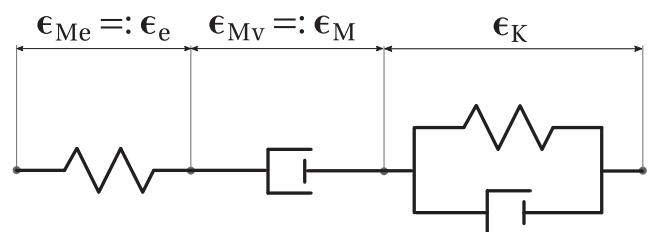


Fig. 1. Generalized linear Burgers model.

it does not allow an unbounded volumetric expansion or compaction during secondary creep. Eqs. (24) to (26) allow the modelling of anisotropic material behavior in the elastic response as well as in primary and secondary creep. Note further, that the expression of an absolute stress in Eq. (24) rather than a stress rate simplifies the implementation of temperature-dependent material properties.

Assuming isotropy, the elasticity tensors can be parametrized according to

$$\mathcal{C}_M = 3K_M \mathcal{P}^S + 2G_M(\mathbf{I} \otimes \mathbf{I} - \mathcal{P}^S) \quad (27)$$

$$\mathcal{C}_K = 3K_K \mathcal{P}^S + 2G_K(\mathbf{I} \otimes \mathbf{I} - \mathcal{P}^S) \quad (28)$$

and the viscosity tensors follow analogously

$$\mathcal{V}_M = 3\eta_{vol M} \mathcal{P}^S + 2\eta_M(\mathbf{I} \otimes \mathbf{I} - \mathcal{P}^S) \quad (29)$$

$$\mathcal{V}_K = 3\eta_{vol K} \mathcal{P}^S + 2\eta_K(\mathbf{I} \otimes \mathbf{I} - \mathcal{P}^S) \quad (30)$$

where usually $\eta_{vol M} \rightarrow \infty$ is chosen to comply with basic physical considerations. For brevity of notation, we have introduced the fourth order spherical and deviatoric projection tensors

$$\mathcal{P}^S = \frac{1}{3} \mathbf{I} \otimes \mathbf{I} \quad (31)$$

$$\mathcal{P}^D = (\mathbf{I} \otimes \mathbf{I})^{\frac{23}{1}} - \mathcal{P}^S \quad (32)$$

where it remains to be noted that in the case of $\mathbf{A} = \mathbf{A}^T$ one can use the identity $\mathbf{A}^D = \mathcal{P}^D : \mathbf{A} = (\mathbf{I} \otimes \mathbf{I} - \mathcal{P}^S) : \mathbf{A}$.

Typical constitutive models of rock salt, such as the LUBBY2 and Minkley models discussed in the sequel, limit the volumetric response of the Burgers model to the elastic member of the Maxwell element with all other rheological elements assumed to undergo deviatoric deformations only.

4. The modified LUBBY2 model

The LUBBY2 model is very common in the geotechnical analysis of rock salt behavior. Here, it is slightly modified for general three-dimensional stress states and its numerical implementation within the above framework is described.

Assuming isotropy and a rate-independent volumetric response, the LUBBY2 model follows from the generalized Burgers model described in the previous section via the following equations

$$\begin{aligned} \boldsymbol{\sigma} &= K_{Me} \mathbf{I} + 2G_M [\boldsymbol{\epsilon}^D - \boldsymbol{\epsilon}_M^D - \boldsymbol{\epsilon}_K^D] \\ \dot{\boldsymbol{\epsilon}}_K^D &= \frac{1}{2\eta_K} (\boldsymbol{\sigma}^D - 2G_K \boldsymbol{\epsilon}_K^D) \\ \dot{\boldsymbol{\epsilon}}_M^D &= \frac{1}{2\eta_M} \boldsymbol{\sigma}^D \end{aligned} \quad (33)$$

4.1. Deviatoric uncoupling of the local system

Considering the generalized Burgers model described in Section 3, the residuals and Jacobians for the local Newton iteration of the stress-update procedure can be computed by resorting to standard 6×6 elasticity and viscosity matrices to represent the corresponding fourth order tensors. This approach allows full flexibility regarding the choice of material parameters as well as the introduction of anisotropic material models. The computation will, however, require many matrix-vector multiplications that can be avoided when certain kinematic restrictions are imposed a priori and isotropic material behavior is assumed. Since these conditions are met for the LUBBY2 model, scalar material parameters can be used instead of the full matrix notation.

As the LUBBY2 model will behave purely elastically for hydrostatic loads, a decoupling of isochoric from volumetric

deformations can be performed making use of the fact that the stresses caused by the latter can be calculated directly without iterative solution techniques:

$$\boldsymbol{\sigma}^S = K_{Me} \mathbf{I} \quad (34)$$

Thus, the local differential-algebraic system (DAE) system will be set up purely in the deviatoric space. In formulating the residual vector defined in Eq. (10) use is made of the Kelvin mapping as outlined in Section 2.2 and Ref. [56]:

$$\mathbf{r}_1 = \frac{\boldsymbol{\sigma}^D}{G_M} - 2[\boldsymbol{\epsilon}^D - \boldsymbol{\epsilon}_K^D - \boldsymbol{\epsilon}_M^D] \quad (35)$$

$$\mathbf{r}_2 = \dot{\boldsymbol{\epsilon}}_K^D - \frac{1}{2\eta_K} (\boldsymbol{\sigma}^D - 2G_K \boldsymbol{\epsilon}_K^D) \quad (36)$$

$$\mathbf{r}_3 = \dot{\boldsymbol{\epsilon}}_M^D - \frac{1}{2\eta_M} \boldsymbol{\sigma}^D \quad (37)$$

with the 18 dimensional state vector $\mathbf{z} = (\boldsymbol{\sigma}^{DT}, \boldsymbol{\epsilon}_K^{DT}, \boldsymbol{\epsilon}_M^{DT})^T$. The tangent matrix extracted from this system by means of Eq. (18) will be related to the deviatoric stress and strain vectors only and has to be extended by the volumetric contribution to be of use in the global iteration:

$$\mathbf{C} = \frac{d\boldsymbol{\sigma}}{d\boldsymbol{\epsilon}} = \frac{d\boldsymbol{\sigma}^D}{d\boldsymbol{\epsilon}^D} \mathcal{P}^D + 3K_M \mathcal{P}^S \quad (38)$$

In analogy to the fourth order tensors \mathcal{P}^D , \mathcal{P}^S , the 6D projection matrices \mathcal{P}^D and \mathcal{P}^S project a 6D vector of tensor components onto its deviatoric and spherical counterpart, respectively.

Note, that in the LUBBY2 formulation the viscosities and the Kelvin shear modulus are functions of the current stress state

$$\eta_M = \eta_{M0} \exp(m_1 \sigma_{eff} / \sigma_0) \quad (39)$$

$$\eta_K = \eta_{K0} \exp(m_2 \sigma_{eff} / \sigma_0) \quad (40)$$

$$G_K = G_{K0} \exp(m_G \sigma_{eff} / \sigma_0) \quad (41)$$

and therefore need to be included in the linearization process of the above functionals when implementing the material model within a Newton-Raphson framework. In the above, parameters with an index 0 denote initial values in the stress free configuration, m_a are material parameters characterising the stress dependency, σ_0 is a reference stress (here, as usually, $\sigma_0 = 1$ MPa) and σ_{eff} follows from Eq. (42).

4.2. Comparison to the classical LUBBY2 model

Two versions of the classical LUBBY2 model exist [22,16]: a time-hardening version which is problematic for several reasons² [22,62] and a strain-hardening version, which is based on the effective quantities

$$\sigma_{eff} = \sqrt{\frac{3}{2}} \boldsymbol{\sigma}^D : \boldsymbol{\sigma}^D \quad \text{and} \quad \boldsymbol{\epsilon}_{Keff} = \sqrt{\frac{2}{3}} \boldsymbol{\epsilon}_K^D : \boldsymbol{\epsilon}_K^D \quad (42)$$

so that, e.g., $\sigma_{Keff}^e = 3G_K \boldsymbol{\epsilon}_{Keff}$. Instead of the full Kelvin strain tensor from Eq. (36), the effective Kelvin strain is taken as an internal variable with the evolution equation

$$\dot{\boldsymbol{\epsilon}}_{Keff} = \frac{1}{3\eta_K} \left(1 - 3G_K \frac{\boldsymbol{\epsilon}_{Keff}}{\sigma_{eff}} \right) \boldsymbol{\sigma}_{eff} \quad (43)$$

This relationship is transformed into a three-dimensional form relying on considerations based on common testing modalities

² Integrating an absolute time measure into constitutive formulations such as the ones discussed here is generally not advisable. In this particular case, the evolution of the viscosity in the case of load reversals or, more generally, in the case of changing boundary conditions could not be described sufficiently based on a time measure but required taking account of the constitutive history [22].

(e.g. triaxial tests) [22,16]. The result is a substitution of the stress and strain quantities outside of the brackets in Eq. (43) by tensorial quantities while leaving the terms within the brackets untouched:

$$\dot{\epsilon}_K^D = \frac{1}{2\eta_K} \left(1 - 3G_K \frac{\epsilon_{Keff}}{\sigma_{eff}} \right) \sigma^D \quad (44)$$

This expression does not correspond to a full 3D formulation of the considered rheological model and clearly contains less information on the inelastic deformation history than the full Burgers model in which the Kelvin strain is expressed by Eq. (33). It can be shown that different solutions will be obtained by the scalar and the full tensorial formulation for certain time-dependent boundary conditions.

In particular, both formulations can yield different results during the transient creep phase while stationary creep is described identically in both models. If scenarios are considered where stationary creep is of primary interest, both formulations can be used without hesitation. If, however, boundary conditions change frequently, e.g. due to loading and unloading, transient creep remains an important influence and the full model formulation (33) is recommended.

The transition performed in Eq. (44) has also affected the nomenclature of material parameters. Therefore, care has to be taken when using material parameters from literature due to a varying interpretation of their meaning that is related to the transition between one-dimensional and three-dimensional states described above and implicitly involve the incompressibility assumption (see Appendix A).

5. A generalized visco-elastoplastic model

Several advanced constitutive models for rock salt are based on the rheological model shown in Fig. 2 consisting of a plastic friction element in series with a Burgers-type model [26–28,31], such that in general

$$\sigma = \mathcal{C}_M : (\epsilon - \epsilon_P - \epsilon_K - \epsilon_M) \quad (45)$$

Making the same material symmetry and kinematic constraints as in the LUBBY2 model but allowing volumetric strains in the plastic element (e.g. dilatant or contractant plastic flow), one can make use of scalar material parameters:

$$\sigma = K_M(e - e_P)\mathbf{I} + 2G_M(\epsilon^D - \epsilon_P^D - \epsilon_K^D - \epsilon_M^D) \quad (46)$$

Several yield surfaces and flow rules have been used to calculate the plastic part of the model, e.g. [28,31]. Since the friction element is in series with the rest of the model and strain softening can occur, the model is prone to localization effects and hence non-physical mesh-dependent results [63,64]. Different remediation strategies exist for this well-known problem. Here, we regularize the general model using a standard Perzyna approach. This matter will not be

discussed further in this contribution; the reader is referred to [55,65,63,66–68] and references therein.

5.1. General implementation

As long as the yield condition is not fulfilled, i.e. $F < 0$, the material behaviour is viscoelastic and the solution method is analogous to that outlined for the Burgers/LUBBY2 models above. This procedure is also used to compute the trial stress with which the yield criterion is evaluated. Upon yielding, we seek the solution to

$$\sigma = K_M(e - e_P)\mathbf{I} + 2G_M(\epsilon^D - \epsilon_P^D - \epsilon_K^D - \epsilon_M^D) \quad (47)$$

$$\dot{\epsilon}_K^D = \frac{1}{2\eta_K} (\sigma^D - 2G_K \epsilon_K^D) \quad (48)$$

$$\dot{\epsilon}_M^D = \frac{1}{2\eta_M} \sigma^D \quad (49)$$

$$\dot{\epsilon}_P^D = \lambda \frac{\partial G_F}{\partial \sigma} : \mathcal{P}^D =: \lambda \mathbf{f}^D \quad (50)$$

$$\dot{e}_P = \lambda \frac{\partial G_F}{\partial \sigma} : \mathcal{P}^S : \mathbf{I} =: \lambda \mathbf{I} : \mathbf{f}^S =: \lambda \dot{f}^S \quad (51)$$

$$\dot{\epsilon}_{Peff} = \sqrt{\frac{2}{3} \dot{\epsilon}_P^D : \dot{\epsilon}_P^D} = \sqrt{\frac{2}{3} \lambda^2 \mathbf{f}^D : \mathbf{f}^D} \quad (52)$$

$$F = 0 \quad (53)$$

The uncoupled treatment of deviatoric and volumetric plastic strains (Eqs. (50) and (51)) is not necessary but is favored here in the context of ongoing model extensions in which a number of parameters depend not only on the plastic arc length ϵ_{Peff} , but also on dilatancy e_P .

Eq. (53) ensures the consistency condition for the rate-independent plastic part. Employing a viscoplastic Ansatz of the Perzyna type [55,65,63] we allow stress states $F > 0$ by introducing a regularization viscosity η_{reg} and set

$$\dot{\epsilon}_P = \frac{\langle \zeta(F) \rangle}{\eta_{reg}} \frac{\partial G_F}{\partial \sigma} \quad (54)$$

A typical formulation for $\zeta(F)$ is

$$\zeta(F) = \left(\frac{F}{C} \right)^n \quad (55)$$

where—to normalize F —a common choices for C is the initial yield stress. For the sake of simplicity, $n = 1$ and $C = G_M$ were chosen here so that the consistency condition in Eq. (53) is replaced by

$$\lambda \eta_{reg} = \langle \zeta(F) \rangle = \frac{\langle F \rangle}{G_M} \quad (56)$$

Note, that a rate-independent formulation is recovered for $\eta_{reg} = 0$.

The corresponding residuals for the stress integration algorithm read with the state vector.

$$\mathbf{z} = (\tilde{\sigma}^T, \epsilon_K^{D,T}, \epsilon_M^{D,T}, \epsilon_P^{D,T}, e_P, \epsilon_{Peff}, \lambda)^T$$

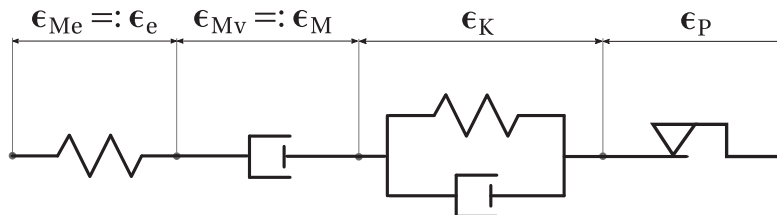


Fig. 2. Rheological analogue of the generalized visco-elastoplastic model.

$$\mathbf{r}_1^j = \tilde{\boldsymbol{\sigma}}^j - \left[2(\boldsymbol{\epsilon}^{Di} - \boldsymbol{\epsilon}_K^{Dj} - \boldsymbol{\epsilon}_M^{Dj} - \boldsymbol{\epsilon}_P^{Dj}) + \frac{K_M}{G_M}(\mathbf{e}^i - \mathbf{e}_P^j) \mathbf{I} \right] \quad (57)$$

$$\mathbf{r}_2^j = \frac{\boldsymbol{\epsilon}_K^{Dj} - \boldsymbol{\epsilon}_K^{Dt}}{\Delta t} - \frac{1}{2\eta_K}(\boldsymbol{\sigma}^{Dj} - 2G_K\boldsymbol{\epsilon}_K^{Dj}) \quad (58)$$

$$\mathbf{r}_3^j = \frac{\boldsymbol{\epsilon}_M^{Dj} - \boldsymbol{\epsilon}_M^{Dt}}{\Delta t} - \frac{1}{2\eta_M}\boldsymbol{\sigma}^{Dj} \quad (59)$$

$$\mathbf{r}_4^j = \frac{\boldsymbol{\epsilon}_P^{Dj} - \boldsymbol{\epsilon}_P^{Dt}}{\Delta t} - \lambda^j \mathbf{f}^D \quad (60)$$

$$\mathbf{r}_5^j = \frac{\mathbf{e}_P^j - \mathbf{e}_P^t}{\Delta t} - \lambda^j \mathbf{f}^S \quad (61)$$

$$\mathbf{r}_6^j = \frac{\boldsymbol{\epsilon}_P^{\text{eff}j} - \boldsymbol{\epsilon}_P^{\text{eff}t}}{\Delta t} - \sqrt{\frac{2}{3}}(\lambda^j)^2 \mathbf{f}^D \cdot \mathbf{f}^D \quad (62)$$

$$\mathbf{r}_7^j = \frac{F}{G_M} - \lambda^j \eta_{\text{reg}} \quad (63)$$

In the above, the dimensionless stress quantity

$$\tilde{\boldsymbol{\sigma}} = \frac{\boldsymbol{\sigma}}{G_M} \quad (64)$$

has been introduced for better algorithmic handling, bringing all residual entries to similar orders of magnitude. Note further the use of the iteration index j attached to quantities to be updated in the local Newton-Raphson loop and is implicit for all quantities that depend on the current state, while the iteration index i is attached to quantities which are iterated in the global Newton-Raphson loop but remain fixed locally; compare Section 2.

The 27×27 Jacobian for the local system defined in Eq. (16) reads

$$\frac{\partial \mathbf{r}}{\partial \mathbf{z}} = \begin{pmatrix} J_{11} & J_{12} & J_{13} & J_{14} & J_{15} & J_{16} & J_{17} \\ J_{21} & J_{22} & J_{23} & J_{24} & J_{25} & J_{26} & J_{27} \\ J_{31} & J_{32} & J_{33} & J_{34} & J_{35} & J_{36} & J_{37} \\ J_{41} & J_{42} & J_{43} & J_{44} & J_{45} & J_{46} & J_{47} \\ J_{51}^T & J_{52}^T & J_{53}^T & J_{54}^T & J_{55} & J_{56} & J_{57} \\ J_{61}^T & J_{62}^T & J_{63}^T & J_{64}^T & J_{65} & J_{66} & J_{67} \\ J_{71}^T & J_{72}^T & J_{73}^T & J_{74}^T & J_{75} & J_{76} & J_{77} \end{pmatrix} \quad (65)$$

where the entries are given in Appendix B.

This implementation can be adjusted to any suitable plasticity model by substituting the corresponding relationships for the yield condition F and the gradients of the plastic potential $\mathbf{f}^D, \mathbf{f}^S$ into Eqs. (60)–(63). In the following section, this will be done for a non-associative Mohr-Coulomb type model.

6. An invariant-based Minkley-type model

Material models of this type have been used to model rock salt behavior in numerous applications over the past years [26–28]. In contrast to the LUBBY2 model, the only parameter in the Burgers part of the model depending on the equivalent stress is the viscosity in the Maxwell element. The following relationship is used³:

$$\eta_M = \frac{\eta_{M0}}{\sinh \left[m \left(\frac{\sigma_{\text{eff}}}{\sigma_0} \right)^n \right]} \quad (66)$$

where m, n are material parameters and σ_0 is a constant reference stress (here, as usually, equal to 1 MPa).

Minkley models rely on a modified Mohr-Coulomb type yield surface. The handling of the multisurface Mohr-Coulomb model under 3D conditions can necessitate 1, 2 (corner) or 6 (apex) plastic multipliers [70]. Furthermore, the usual formulation in principal space hinders an efficient implementation and the linearization

of the eigenprojections $\mathbf{n}^{(i)} \otimes \mathbf{n}^{(i)}$ occurring in the plastic flow-rule is nontrivial, especially for repeated eigenvalues [42,71–73]. Thus, only plasticity models in invariant formulation based on

$$\begin{aligned} I_1 &= \text{tr} \boldsymbol{\sigma} & J_2 &= \frac{1}{2} \boldsymbol{\sigma}^D : \boldsymbol{\sigma}^D & J_3 &= \det \boldsymbol{\sigma}^D \\ \theta &= \frac{1}{3} \arcsin \left(-\frac{3\sqrt{3}J_3}{2\sqrt{J_2^3}} \right) \end{aligned} \quad (67)$$

will be considered here where the last definition refers to the Lode angle with $-\frac{\pi}{6} \leq \theta \leq \frac{\pi}{6}$ [64,74]. At the singularities of the yield surface the gradient with respect to the stresses is undefined which can cause problems in simulations, esp. those on axisymmetric meshes [69]. Several corner smoothing approaches are available, e.g. [45,69,70]. The function proposed by Sloan and Booker [69] has a simple structure, provides a smooth transition between the standard and the modified formulation, and can approximate the classical Mohr-Coulomb surface near the corners to various degrees controlled by one transition angle θ_T (Fig. 3). In order to remain as close as possible to the original Mohr-Coulomb formulation used in, e.g., [26], this approach has been favored here.

The yield function reads [69]

$$F = \begin{cases} \frac{1}{3} \sin \phi + \sqrt{J_2} \left(\cos \theta - \frac{1}{\sqrt{3}} \sin \phi \sin \theta \right) - c \cos \phi & |\theta| < \theta_T \\ \frac{1}{3} \sin \phi + \sqrt{J_2} (A - B \sin 3\theta) - c \cos \phi & |\theta| \geq \theta_T \end{cases} \quad (68)$$

where c and ϕ are the cohesion and friction angle, respectively, and

$$A = \frac{1}{3} \cos \theta_T \left[3 + \tan \theta_T \tan 3\theta_T + \frac{1}{\sqrt{3}} \text{sign}(\theta) (\tan 3\theta_T - 3 \tan \theta_T) \sin \phi \right] \quad (69)$$

$$B = \frac{1}{3} \frac{1}{\cos 3\theta_T} \left[\text{sign}(\theta) \sin \theta_T + \frac{1}{\sqrt{3}} \sin \phi \cos \theta_T \right] \quad (70)$$

The plastic potential differs from the yield surface in order to more accurately estimate dilatancy, but has an analogous structure:

$$G_F = \begin{cases} \frac{1}{3} \sin \psi + \sqrt{J_2} \left(\cos \theta - \frac{1}{\sqrt{3}} \sin \psi \sin \theta \right) & |\theta| < \theta_T \\ \frac{1}{3} \sin \psi + \sqrt{J_2} (A' - B' \sin 3\theta) & |\theta| \geq \theta_T \end{cases} \quad (71)$$

where ψ is the dilatancy angle. A' and B' follow from Eqs. (69) and (70) by substituting the friction angle with the dilatancy angle.

Plastic flow follows in a general manner for a I_1, J_2, θ -type yield surface

$$\dot{\boldsymbol{\epsilon}}_P = \lambda \frac{\partial G_F}{\partial \boldsymbol{\sigma}} = \lambda \left[\frac{\partial G_F}{\partial I_1} \mathbf{I} + \left(\frac{\partial G_F}{\partial J_2} + \frac{\partial G_F}{\partial \theta} \frac{\partial \theta}{\partial J_2} \right) \boldsymbol{\sigma}^D + \frac{\partial G_F}{\partial \theta} \frac{\partial \theta}{\partial J_3} J_3 (\boldsymbol{\sigma}^D)^{-1} : \boldsymbol{\mathcal{P}}^D \right] \quad (72)$$

Commonly, nonlinear history-dependent friction and dilatancy functions are introduced to characterize the complex behavior of rock salt in the works of Minkley et al. [27,26,28,29]. This coupling is important for the description of softening and dilatancy phenomena under changing stress and deformation states [3]. The dependencies in the cited works [26–29] can be transformed and expressed via the general functions

$$c = \tilde{c}(\boldsymbol{\sigma}, \epsilon_P^{\text{eff}}) \quad (73)$$

$$\phi = \tilde{\phi}(\boldsymbol{\sigma}, \epsilon_P^{\text{eff}}) \quad (74)$$

$$\psi = \tilde{\psi}(\boldsymbol{\sigma}, \epsilon_P^{\text{eff}}) \quad (75)$$

thus transforming the complex yield surface and plastic potentials locally to Mohr-Coulomb-type formulations. Here, our purpose is to show the algorithmic implementation into an implicit finite

³ To get a constant viscosity $\eta_M = \eta_{M0}$ choose $m = \ln(1 + \sqrt{2})$ and $n = 0$.

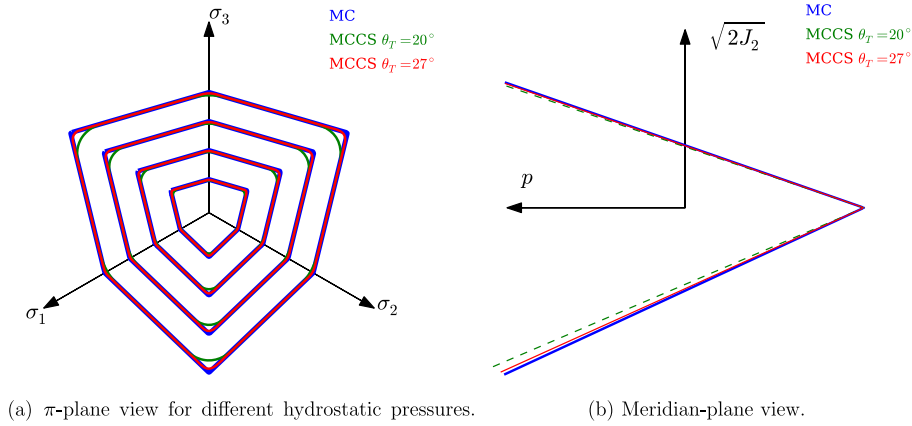


Fig. 3. Comparison the classical Mohr-Coulomb yield surface (blue) and the yield surface obtained by the corner smoothing approach [69] for two different transition angles (green, red). A friction angle of 25° was used for the plots. (For interpretation of the references to colour in this figure legend, the reader is referred to the web version of this article.)

element code. Therefore, we only introduce isotropic hardening/softening via the relation

$$c = c_0(1 + H\epsilon_{p\text{ eff}}) \quad (76)$$

More complex dependencies can of course be added following the approach described herein.

The linearization of the described model for the local Newton-Raphson procedure in the context of the generalized viscoplastic model described in Section 5 can be found in Appendix C.

7. Implementation verification

7.1. Simple shear creep

The purpose of this benchmark was to test the implementation of the Burgers-part of both the LUBBY2 and the Minkley model as well as their parameters' stress and temperature dependencies. For that purpose, yielding was excluded in the Minkley model by setting the cohesion to a very high value.

Simple shear was chosen as a test case. Following a stress jump, the analytical solution for the shear strain developing in a Burgers-type model reads:

$$\epsilon_{xy}(t) = \frac{1}{2}\gamma_{xy}(t) = \frac{1}{2}\left[\left(\frac{1}{G_M} + \frac{1}{\eta_M}t\right)\sigma_{xy} + \frac{1}{G_K}\left(1 - e^{-\frac{G_K t}{\eta_K}}\right)\sigma_{xy}\right] \quad (77)$$

Note, that in the LUBBY2 formulation the viscosities and the Kelvin shear modulus are functions of the current stress state (Eqs. (39)–(41)) where under the considered conditions

$$\sigma_{\text{eff}} = \sqrt{3\sigma_{xy}^2} \quad (78)$$

To describe the temperature dependence of the solution, the elastic properties varied linearly with a temperature change with respect to a reference temperature T_{ref} [75]:

$$K_M = K_{M0} + m_{KT}(T - T_{\text{ref}}) \quad G_M = G_{M0} + m_{GT}(T - T_{\text{ref}}) \quad (79)$$

The Maxwell viscosity describing the stationary creep rate varied based on an Arrhenius-type relationship [76] in addition to its stress dependency:

$$\eta_M = \eta_{M0} \exp[m_1 \sigma_{\text{eff}} / \sigma_0] \exp[Q(T_{\text{ref}} - T) / (RTT_{\text{ref}})] \quad (80)$$

In the above, R is the universal gas constant. As simple shear is a strictly isochoric test, a temperature increase will lead to a hydrostatic pressure developing in the sample due to the suppressed thermal volume strain. This pressure is analytically given by

$$p = K_M 3\alpha_T(T - T_{\text{ref}}) \quad (81)$$

The parameters in Tables 1 and 2 are used. A shear stress of $\sigma_{xy} = 5$ MPa is numerically imposed in 0.01 days and held for 25 days. At day 15, the temperature is quickly and homogeneously increased from 313 to 373 K. The numerical solution was obtained by subjecting a single 2D eight-node quadrilateral finite element to simple shear loading.

In the Minkley formulation, only the Maxwell viscosity is stress-dependent following Eq. (66). The temperature dependence of the elastic properties followed Eq. (79) and the Maxwell viscosity was extended by a temperature dependence analogous to Eq. (80):

$$\eta_M = \frac{\eta_{M0} \exp[Q(T_{\text{ref}} - T) / (RTT_{\text{ref}})]}{\sinh\left[m\left(\frac{\sigma_{\text{eff}}}{\sigma_0}\right)^n\right]} \quad (82)$$

The material parameters used can be found in Tables 3 and 2. A shear stress of $\sigma_{xy} = 2$ MPa is numerically imposed in 1 day and held for 2500 days. At day 1500, the temperature is quickly and homogeneously increased from 313 to 373 K.

In both tests, the local absolute tolerance (for the respective Euclidean vector norms) was set to 10^{-14} , while the absolute displacement increment tolerance was set to 10^{-8} . Analytical and numerical solution fit well for both models (Fig. 4a and b): the maximum absolute error of the shear strain remained below $3 \cdot 10^{-6}$ while the maximum absolute deviation of the hydrostatic pressure was on the order of $3 \cdot 10^{-2}$ Pa. The initial instantaneous deformation is followed by the transition from transient to stationary creep after load application. Once the temperature is increased, the sudden drop of the Maxwell shear modulus leads to an instantaneous increase in shear strain followed by stationary creep at a higher rate due to the lowered Maxwell viscosity. The temperature rise in combination with the isochoric confinement of the sample causes a significant hydrostatic pressure which is determined by the temperature dependent Maxwell bulk modulus of the material and the thermal expansion coefficient.

Table 1

Temperature-independent material parameters for the LUBBY2 model; Eqs. (33) and (39)–(41). The mass density was set to 2200 kg m^{-3} . Parameters from [30,22]. Parameters describing temperature dependence are listed in Table 2.

G_{M0} (MPa)	K_{M0} (MPa)	η_{M0} (MPa d)	G_{K0} (MPa)
$9.54 \cdot 10^3$	$2.78 \cdot 10^4$	$4.03 \cdot 10^7$	$6.27 \cdot 10^4$
η_{K0} (MPa d)	m_1 (MPa $^{-1}$)	m_2 (MPa $^{-1}$)	m_G (MPa $^{-1}$)
$1.66 \cdot 10^5$	−0.327	−0.267	−0.254

Table 2

Materials describing the temperature dependence of the elastic properties, Eq. (79) and Ref. [75], and the stationary creep rate, Eq. (80) and Ref. [76].

m_{CT} (MPa K ⁻¹)	m_{KT} (MPa K ⁻¹)	Q (J mol ⁻¹)	T_{ref} (K)	α_T (K ⁻¹)
-21.141	-25.265	$1.6 \cdot 10^4$	313	$2.8 \cdot 10^{-5}$

Table 3

Temperature-independent material parameters for the Minkley model, Eqs. (47)–(53), (66), (68)–(71). Information on parameter identification can be found in [29]. Parameters describing temperature dependence are listed in Table 2.

G_M (MPa)	K_M (MPa)	η_{M0} (MPa d)	G_{K0} (MPa)	η_{K0} (MPa d)	m (MPa ⁻ⁿ)
$1.2 \cdot 10^4$	$1.8 \cdot 10^4$	$10.0 \cdot 10^{10}$	$6.3 \cdot 10^4$	$1.4 \cdot 10^7$	4.9
n	c_0 (MPa)	h	ϕ (°)	ψ (°)	η_{reg}
0.33	1.6	100.0	20.0	5.0	0.01

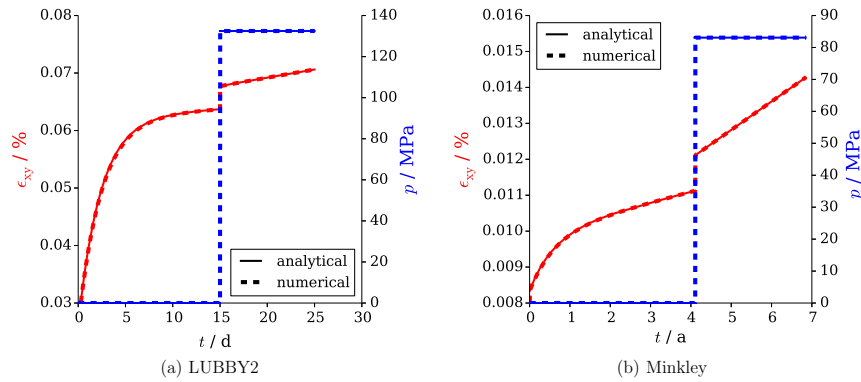


Fig. 4. Results of a simulated simple shear creep test for the LUBBY2 model run with parameters from Table 1 and the Minkley model with parameters from Table 3. About half-way through the test, a temperature jump was imposed causing an immediate change in the elastic response visible as a jump in the shear strain curve (red), a significant hydrostatic pressure (blue) due to isochoric confinement of the sample, as well as an increased creep rate. Parameters describing temperature dependence see Table 2. Comparison of numerical and analytical solutions, cf. Eqs. (77) and (81). The maximum absolute error of the shear strain remained below $3 \cdot 10^{-6}$ (0.6% relative error) while the maximum absolute deviation of the hydrostatic pressure was on the order of $3 \cdot 10^{-2}$ Pa ($2 \cdot 10^{-8}\%$). Time units days (d) and years (a). (For interpretation of the references to colour in this figure legend, the reader is referred to the web version of this article.)

7.2. Elastoplastic response of a circular hole to repeated loading

As the viscoelastic part of the implementation has been verified in the previous section, this section focusses on the elasto-plastic part of the Minkley model. For that purpose, the parameters η_{M0} , η_{K0} , and G_{K0} are set to very high values, reducing the model to a classical Mohr-Coulomb rate-independent plasticity model ($\eta_{reg} = 0$).

The analytical solution given in Senseny et al. [77]⁴ for a circular hole in an infinite medium under plane strain conditions was approximated numerically using an axisymmetric mesh with an inner radius of 1 m representing the hole and an outer radius of 21 m (see Fig. 5) which is far enough from the hole to approximate the infinite medium. The mesh consisted of 150 8-noded quadrilateral finite elements in the radial direction. The cavity wall was modelled traction-free while at the outer boundary an axisymmetric pressure load was prescribed in 4 stages:

- Stage I: 15 MPa were applied in 10 equal load steps.
- Stage II: The load was completely removed in 10 equal load steps.
- Stage III: 15 MPa were re-applied in 10 equal load steps, leading to additional convergence of the hole in comparison to stage I.
- Stage IV: The load was increased to 20 MPa in 10 equal load steps.

A Young's modulus of $E = 6778$ MPa, a Poisson's ratio of $\nu = 0.21$, a constant cohesion of $c_0 = 3.45$ MPa and a friction angle

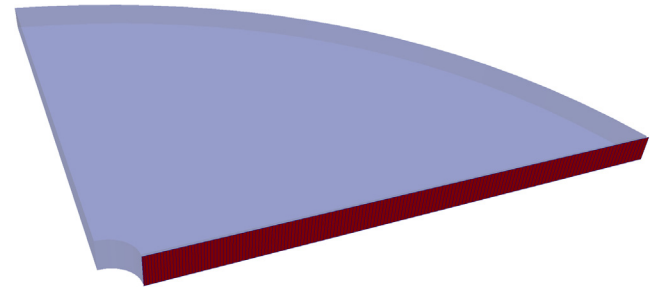


Fig. 5. Schematic representation of the circular hole in an elasto-plastic medium used for the verification of the numerical implementation based on the analytical solution from Ref. [77]. A 3D impression using quarter symmetry is shown in blue, the axisymmetric mesh used for the numerical simulation is depicted in red. (For interpretation of the references to colour in this figure legend, the reader is referred to the web version of this article.)

of $\phi = 30^\circ$ were used. Associative flow was employed. Non-associativity was validated for Stage I by adapting the analytical solution accordingly and using a dilatancy angle $\psi = 0^\circ$ [77].

The resulting stresses and radial displacements in the near-field of the hole can be seen in Fig. 6. Based on the chosen discretization, numerical and analytical displacements showed maximum absolute deviations of 0.015 mm, 0.002 mm, 0.015 mm and 0.9 mm at the end of stages I, II, III, and IV, respectively. The slight inaccuracy during stage IV in the displacement solution likely stems from the fact that the problem is stress-controlled and a non-linear material model is employed to calculate plastic deviatoric and volumetric strains under an axisymmetry constraint.

⁴ In Eqs. (13) of Ref. [77], $+P_R$ has to be used instead of $-P_R$.

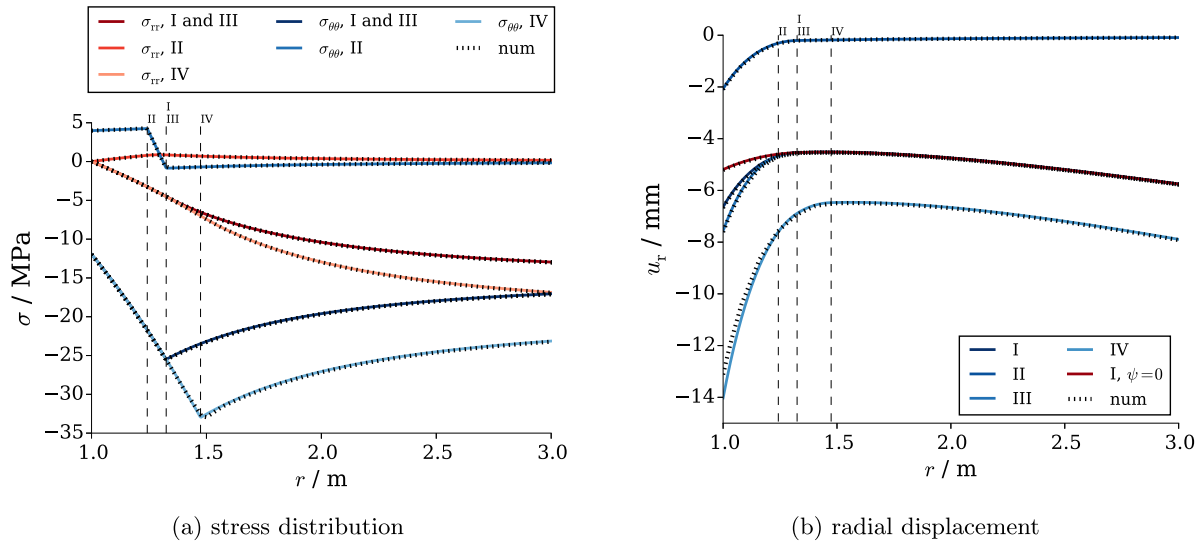


Fig. 6. (a) Radial and circumferential stresses and (b) radial displacements. Comparison of numerical (dotted lines) and analytical solutions [77] for repeated loading of a circular hole in a Mohr-Coulomb medium. Vertical dashed lines indicate the current radius of the moving plastic zones at the end of the various stages. Based on the chosen discretization, numerical and analytical displacements showed maximum absolute deviations of 0.015 mm, 0.002 mm, 0.015 mm and 0.9 mm at the end of stages I (both for associated and non-associated flow), II, III, and IV, respectively. The stress distribution during stage I represents both the curves for associated and non-associated flow.

8. Numerical convergence behavior

8.1. Algorithmic convergence

To test the numerical behavior of the algorithm, several simulations were performed. For a basic convergence analysis, a generic triaxial test was simulated using the parameter set from Table 3. Rather than modelling a specific laboratory experiment, the loading protocol was set up such that all material effects were active to achieve a convergence analysis of the entire algorithm. The following load steps, each divided into ten equal time steps, were used:

- Application of a radial confining stress of -4 MPa within 2 days.
- Application of -0.1% axial strain within 2 days.
- Hold all boundary conditions for 200 days.
- Reduction of the axial strain to -0.07% within 2 days.
- Hold all boundary conditions for 200 days.
- Increase axial strain back to -0.1% within 2 days.
- Increase radial confining stress to -8 MPa within 2 days.
- Increase axial strain to -0.25% within 2 days.

Furthermore, to demonstrate the possibility of a transition from hardening to softening behavior, the hardening law was extended to read

$$c = c_0(1 + H\epsilon_{p\text{ eff}} + H_2\epsilon_{p\text{ eff}}^2 + H_4\epsilon_{p\text{ eff}}^4) \quad (83)$$

where for illustration the following values were set: $H_2 = -1 \cdot 10^{-5}$ and $H_4 = -5 \cdot 10^{-10}$. Contact to the loading platens was assumed to be frictionless in order to achieve a homogenous deformation state throughout the cylindrical sample without barrelling so that one 8-node biquadratic axisymmetric finite element was sufficient for discretization.

The results show the transition from the viscoelastic to a viscoplastic hardening behavior during the first strain application-phase which is accompanied by the occurrence of dilatancy (Fig. 7). Stress relaxation with a decreasing stress can be observed during the subsequent hold phase. Stress relaxation during the hold phase which follows the partial unloading of the sample, in contrast, shows an increasing stress. The final loading stage ex-

hibits the transition from hardening behavior to softening which quickly progresses with strain.

During the entire test, quadratic convergence is observed both at the integration point level and of the displacement-based FEM formulation (Fig. 8). The convergence test clearly shows the increased non-linearity once yielding occurs while during the hold phases convergence was very rapid.

8.2. Example simulations

A disc-with-a-hole test was simulated using a 2D mesh consisting of 2550 quadrilateral 8-node elements. The disc had dimensions of 20 m times 20 m and a central hole with a diameter of 2 m. Half symmetry and the plane strain assumption were employed. The normal displacements of the bottom edge were constrained while at the top a pressure of 7 MPa was applied within one day in ten time steps and held for another 10 + 100 + 1000 days (total duration short of 3.5 years) with each interval

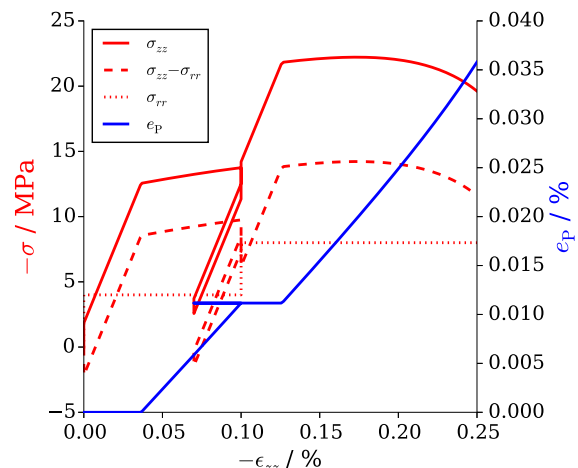


Fig. 7. Axial stress, differential axial stress and dilatancy over axial strain for the triaxial test.

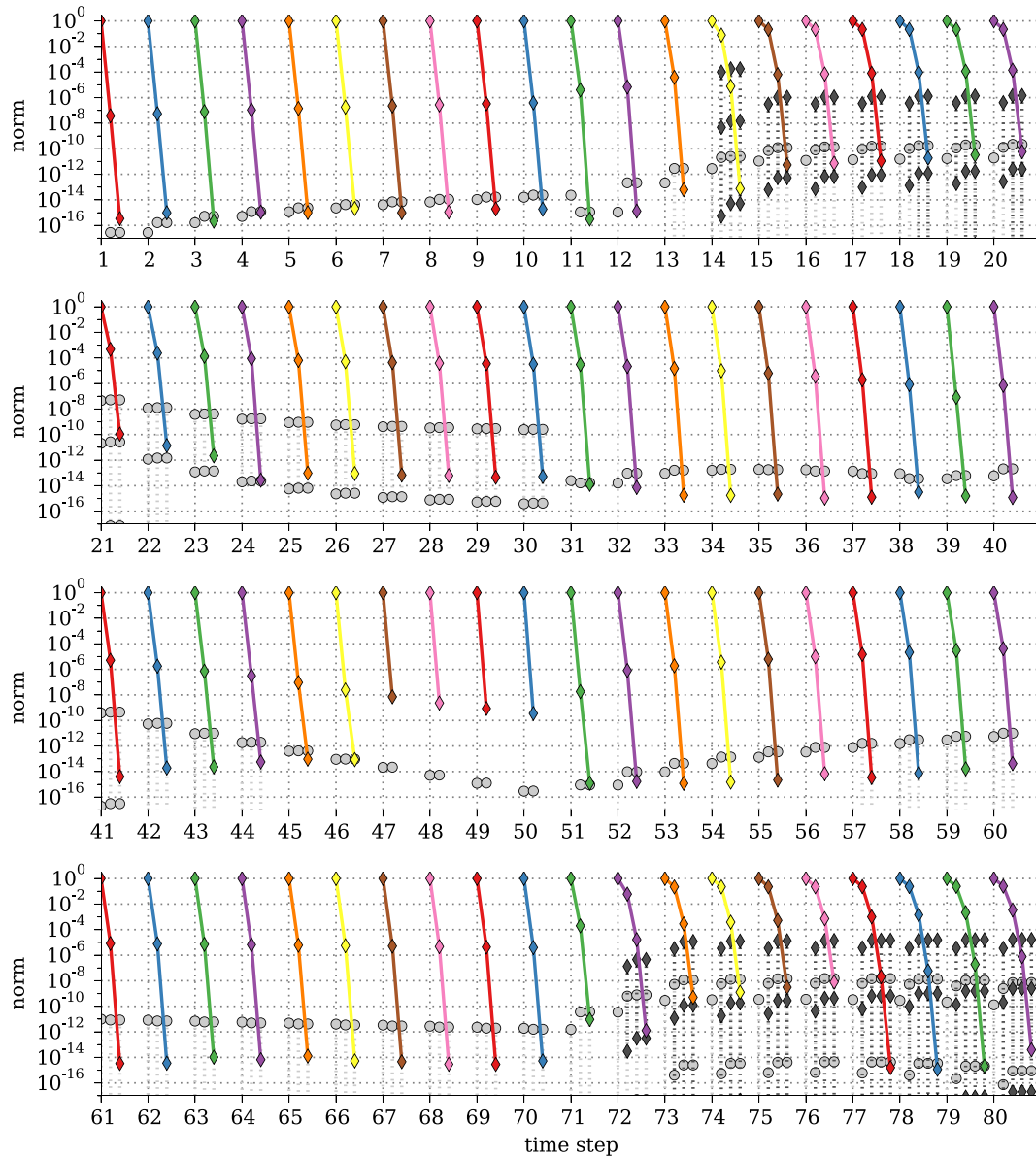


Fig. 8. Convergence of the global and local Newton iterations during the eight load steps of the triaxial test (Fig. 7). Each load step took 10 time steps. The norm of the global residual vector $\|\Delta\psi\|/\|\Delta\psi_0\|$ is shown in solid colored lines with diamond markers. Global convergence was achieved if $\|\Delta\psi\|/\|\Delta\psi_0\| < 10^{-8}$ and $\|\Delta u\|/\|\Delta u_0\| < 10^{-8}$, i.e. if both relative force and displacement residuals dropped below a given tolerance. The lines connect the successive global iterations in a time step. Beneath each global iteration, the gray dotted lines with circular markers show the norms of the local residuals $\|r\|$ during integration of the viscoelastic trial stress. Dark gray lines connecting diamond markers show the norms of the local residuals $\|r\|$ during integration of the complete viscoplastic model and are thus an indication of the time steps during which dilatant yielding occurred. Convergence of the local system was achieved if $\|r\| < 10^{-12}$. The local residual was evaluated in one integration point of the finite element. (For interpretation of the references to colour in this figure legend, the reader is referred to the web version of this article.)

divided into ten equal time steps. Prior to load application, gravity was applied within one time step of 10 days. For the lateral edge, two types of boundary conditions were investigated:

- *Displacement boundary condition:* The lateral edge was constrained in its normal direction.
- *Traction boundary condition:* The lateral edge was subjected to a normal traction linearly increasing with depth according to lithostatic conditions and starting at 7 MPa at the top corner. This boundary condition was linearly increased over the first day of the simulation with the same time curve as the top pressure.

Load magnitudes and geometry were chosen to lie in a realistic range (e.g. a tunnel in rock salt). The simulation was performed using the parameters given in Table 3.

To test whether the solution based on the standard mesh (2550 elements) was sufficient to represent the complex plastic behavior, the simulation was repeated with a refined mesh using 25,200 second-order elements. Time stepping was kept unchanged. The result is shown in Fig. 9. The predicted values for dilatancy differ only slightly and both meshes clearly show the dilatant regions along with the developing shear bands in the case of the displacement boundary conditions. Shear band location, extension and width agree well. For a more quantitative comparison, certain results were compared along a line extending horizontally outwards from the midpoint of the tunnel.

The relative error between coarse and fine solution mostly stayed within $\pm 1.5\%$, except for the first principal stress when approaching the cavity (Fig. 10). This stress corresponds here to the radial stress for which there is a homogeneous Neumann

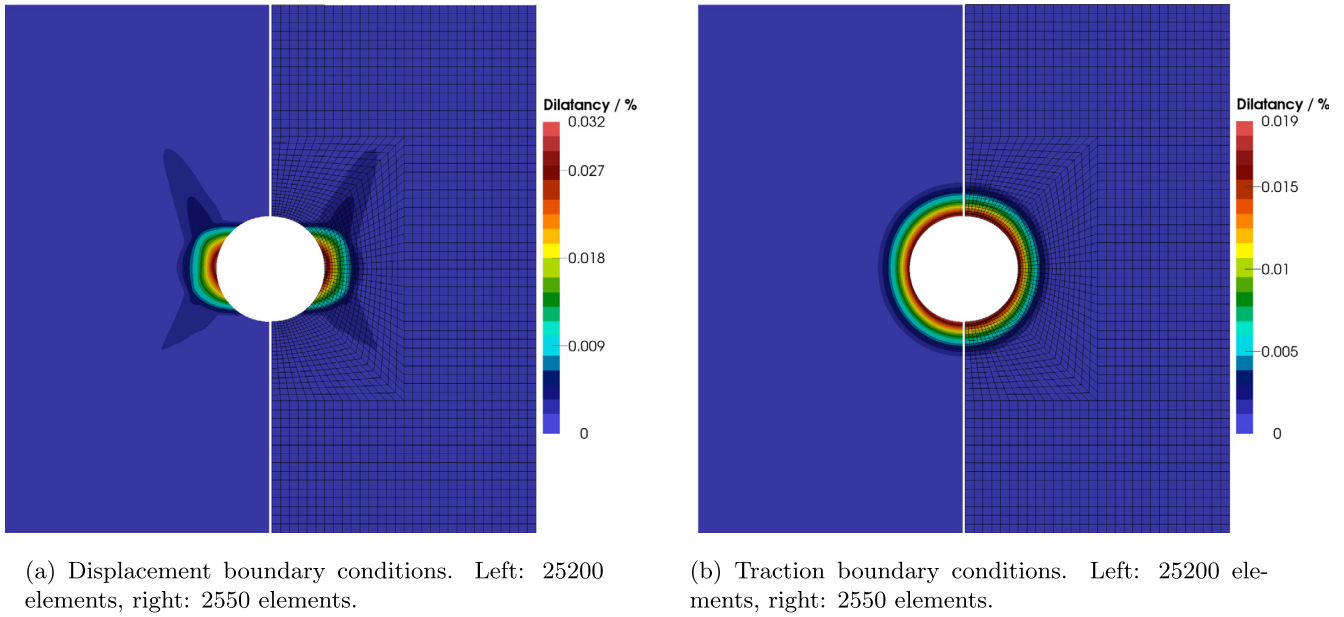


Fig. 9. Dilatancy (in %) (at maximum compression) for the tunnel example using the Minkley implementation. Both meshes predict very similar values for the dilatancy. While the plastic zone is circular for the case with traction boundary conditions, shear band-like structures are beginning to develop in the case with displacement boundary conditions. For reasons of visibility, only the coarse mesh is shown.

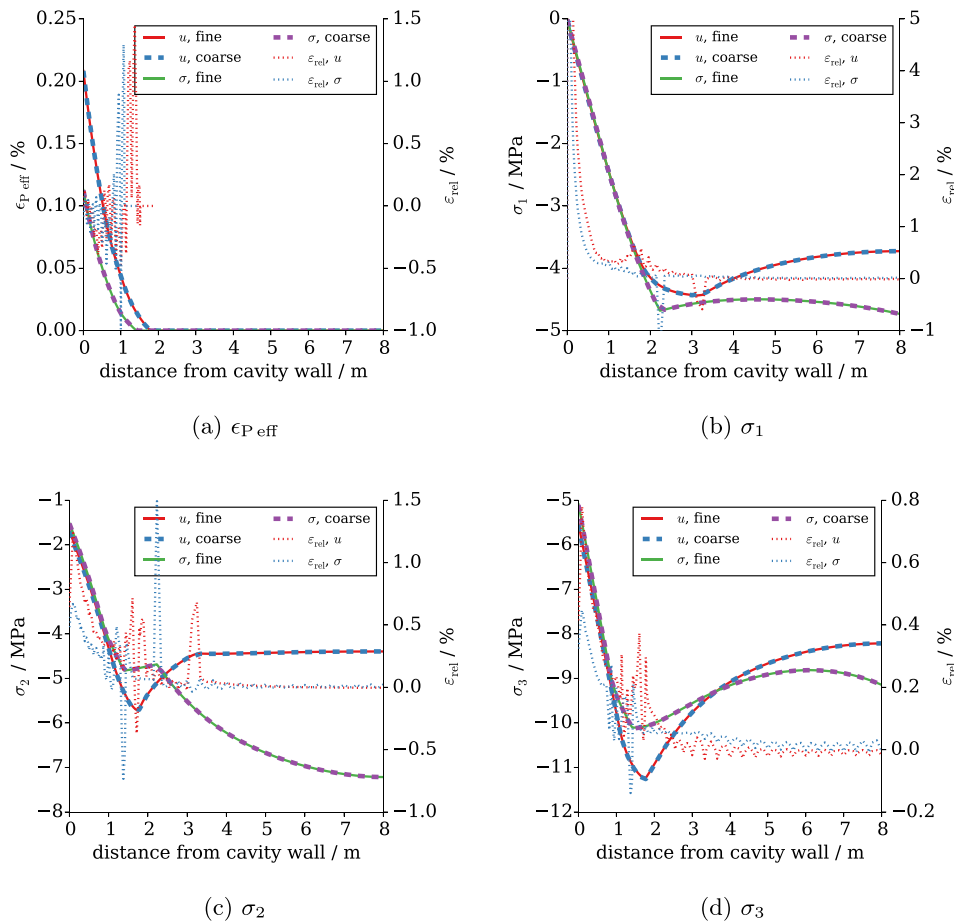


Fig. 10. Comparison of the effective plastic strain and the principal stresses computed along a line extending horizontally outwards from the cavity wall for the fine mesh and the coarse mesh for both types of boundary conditions. The dotted lines represent the relative error between the coarse and the fine solution given in per cent.

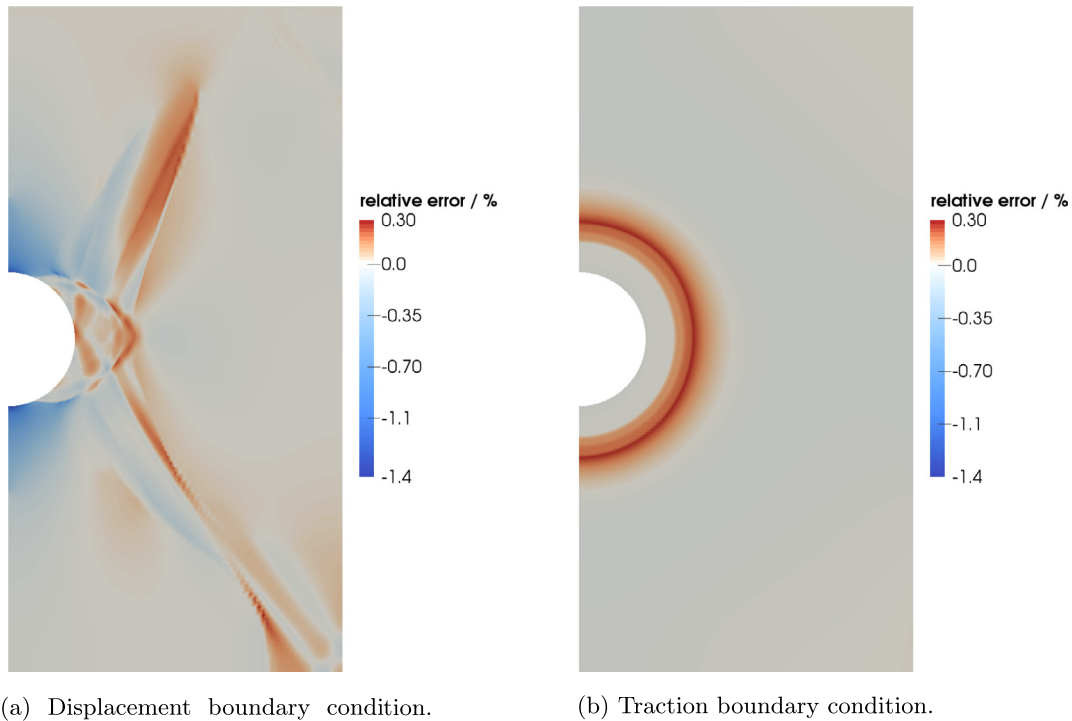


Fig. 11. Relative error $\epsilon_{\text{rel}} = (\sigma_3^{\text{coarse}} - \sigma_3^{\text{fine}}) / \sigma_3^{\text{fine}}$ in per cent of the third principal stress between a coarse and fine time discretization.

boundary condition in at the cavity wall. The interpolation of the stress results to the cavity wall approaching the boundary condition value strongly depends on the available mesh resolution which explains the increased errors in this zone.

Finally, the fine mesh was used to check the effect of the time step size. For that purpose, the total number of time steps was increased from 40 to 400 by dividing the time step size in each of the above mentioned intervals by ten. Similar to mesh convergence, the results from both simulations agreed quite well. In Fig. 11, the relative error for the third principal stress (maximum compressive stress) is plotted. In most regions, it remained well below 1%. It was slightly elevated around the cavity, and in the regions undergoing plastic deformation. It can also be noted that the relative error contours follow the developing shear bands in the case of the simulation with displacement boundary conditions (Fig. 11b).

9. Concluding remarks

The implementation of the LUBBY2 and Minkley models within an implicit time integration scheme into the scientific open-source finite element code OpenGeoSys has been presented. All derivatives necessary for the implementation in the context of a Newton-Raphson scheme using an analytical Jacobian have been provided. The implementation has been verified by comparison against analytical solutions of thermomechanical problems and the convergence behavior has been illustrated using a set-up inspired by a tunnel in rock salt formations. While implicit time integration of inelastic constitutive models is well developed methodologically [39–46,48–52], to the best of the authors' knowledge, this is the first detailed investigation of the frequently used LUBBY2 and Minkley models in an implicit scheme in the literature. The significance of this effort is rooted in the widespread use of these models in large-scale geotechnical projects and the robustness of implicit methods [41]. The use of the Kelvin mapping is not standard in the literature but significantly simplifies the implementation process for reasons outlined in [56]. Finally, a con-

sistent treatment of the material parameters for the LUBBY2 model known from the literature has been illustrated avoiding confusion when switching from 1D to 3D settings.

The small strain assumption can become invalid for extended creep durations, especially in the near-field of geotechnical installations. There is a need for extending the existing rock salt models to finite deformations and for providing suitable numerical methods for their solution in common geotechnical software. Currently, such features are being included into the next version of the OpenGeoSys framework.

At present, the implementation is extended to capture in a more detailed fashion the nonlinearities observed in rock salt [28,29]. Large-scale simulations of inelastic material models can be computationally very challenging. In the present implementation, simulations can be performed taking benefit of an already existing parallelization scheme [78,79]. Furthermore, couplings to hydraulic processes (percolation) will be taken into account [3].

Acknowledgments

The authors would gratefully like to acknowledge the funding provided by the German Ministry of Education and Research (BMBF) for the ANGUS+ project, Grant No. 03EK3022, as well as the support of the Project Management Jülich (PtJ). Additional funding was provided by the Helmholtz Initiating and Networking Fund through the NUMTHECHSTORE project.

Appendix A. Material parameter conversion for LUBBY2

The parameterization of the inelastic part of the constitutive model has often relied on a combination of tests under uniaxial and triaxial test configurations in which different material parameters have been determined, e.g. G_K and \bar{G}_K [22,30]. Specifically, this led to the definition of different shear moduli and viscosities for uniaxial (•) and three dimensional stress analyses (•) which we consider to be an abuse of nomenclature and the cause of some confusion:

$$3G_K = \bar{G}_K \quad 3\eta_K = \bar{\eta}_K \quad 3\eta_M = \bar{\eta}_M \quad (\text{A.1})$$

This conversion has its root in an unusual definition of material parameters in the uniaxial case and requires clarification. The inelastic constitutive model (Kelvin element and Maxwell dashpot) has been assumed to permit only isochoric deformations. The distortional strain energy leads to the definition of equivalent scalar stresses and strains under the assumption of elasticity (here: $\sigma^D = 2G\epsilon^D$):

$$\psi_{\text{iso}} = \frac{1}{2} \sigma^D : \epsilon^D = G \epsilon^D : \epsilon^D = \frac{1}{2} \sigma_{\text{eff}} \epsilon_{\text{eff}} \quad \text{with} \quad \sigma_{\text{eff}} = \sqrt{\frac{3}{2} \sigma^D : \sigma^D} \quad \text{and} \quad \epsilon_{\text{eff}} = \sqrt{\frac{2}{3} \epsilon^D : \epsilon^D} \quad (\text{A.2})$$

The deviatoric stress in a linear spring or dash pot can be calculated as

$$\sigma^D = 2G\epsilon^D \quad \text{and} \quad \sigma^D = 2\eta\dot{\epsilon}^D \quad (\text{A.3})$$

Consider now a uniaxial stress state where only $\sigma_{11} \neq 0$. Then,

$$\sigma_{\text{eff}} = \sigma_{11} \quad \text{and} \quad \epsilon_{\text{eff}} = \frac{2}{3}(1+\nu)\epsilon_{11} \stackrel{\nu=0.5}{=} \epsilon_{11} \quad (\text{A.4})$$

where $\nu = 0.5$ corresponds to the incompressibility assumption. An unconfined compressive test will, according to Hooke's law, determine the Young's modulus (or a similarly defined viscosity measure):

$$\sigma_{11} = E\epsilon_{11} \quad (\text{A.5})$$

We can rewrite this equation using effective quantities

$$\sigma_{\text{eff}} = \frac{3E}{2(1+\nu)} \epsilon_{\text{eff}} = 3G\epsilon_{\text{eff}} \stackrel{\nu=0.5}{\rightarrow} \sigma_{\text{eff}} = E\epsilon_{\text{eff}} \quad (\text{A.6})$$

With the incompressibility assumption remaining implicit, the 1D tests in [22,30] were evaluated in terms of E (and equivalent viscosity measures) which was termed \bar{G} . Therefore,

$$\sigma^D = 2G\epsilon^D = 2\frac{E}{2(1+\nu)}\epsilon^D \stackrel{\nu=0.5}{=} 2\frac{E}{3}\epsilon^D = 2\frac{\bar{G}}{3}\epsilon^D \rightarrow \bar{G} = 3G \quad (\text{A.7})$$

Here, we suggest to stick to a standard nomenclature and not introduce any of the quantities denoted with a bar. Additionally, care must be taken when using material parameters from the salt mechanics literature to ensure the “correct” shear modulus/viscosity is used.

Appendix B. Local Jacobian of the generalised viscoplastic model

Row 1:

$$J_{11} = I, \quad J_{12} = J_{13} = J_{14} = 2I, \quad J_{15} = \frac{K_M}{G_M} I, \quad J_{16} = J_{17} = 0 \quad (\text{B.1})$$

Row 2:

$$J_{21} = -\frac{G_M}{2\eta_K} \mathbf{p}^D, \quad J_{22} = \left(\frac{1}{\Delta t} + \frac{G_K}{\eta_K} \right) I, \quad J_{23} = J_{24} = 0, \quad J_{25} = J_{26} = J_{27} = 0 \quad (\text{B.2})$$

Row 3:

$$J_{31} = -\frac{G_M}{2\eta_M} \mathbf{p}^D + \frac{\sigma^{Dj}}{2\eta_M^2} \otimes \frac{\partial \eta_M}{\partial \sigma}, \quad J_{32} = 0, \quad J_{33} = \frac{1}{\Delta t} I, \quad J_{34} = 0, \quad J_{35} = J_{36} = J_{37} = 0 \quad (\text{B.3})$$

Row 4:

$$J_{41} = -\lambda^j \frac{\partial \mathbf{f}^D}{\partial \tilde{\sigma}^j}, \quad J_{42} = J_{43} = 0, \quad J_{44} = \frac{1}{\Delta t} I - \lambda^j \frac{\partial \mathbf{f}^D}{\partial \epsilon_p^{Dj}}, \quad J_{45} = -\lambda^j \frac{\partial \mathbf{f}^D}{\partial \epsilon_p^j}, \quad J_{46} = -\lambda^j \frac{\partial \mathbf{f}^D}{\partial \epsilon_{p \text{ eff}}^j}, \quad J_{47} = -\mathbf{f}^D \quad (\text{B.4})$$

Row 5:

$$J_{51} = -\lambda^j \frac{\partial \mathbf{f}^S}{\partial \tilde{\sigma}^j}, \quad J_{52} = J_{53} = 0, \quad J_{54} = -\lambda^j \frac{\partial \mathbf{f}^S}{\partial \epsilon_p^{Dj}}, \quad J_{55} = \frac{1}{\Delta t} - \lambda^j \frac{\partial \mathbf{f}^S}{\partial \epsilon_p^j}, \quad J_{56} = -\lambda^j \frac{\partial \mathbf{f}^S}{\partial \epsilon_{p \text{ eff}}^j}, \quad J_{57} = -\mathbf{f}^S \quad (\text{B.5})$$

Row 6:

$$J_{61} = -\frac{2(\lambda^j)^2}{3\sqrt{\frac{2}{3}(\lambda^j)^2 \mathbf{f}^D \cdot \mathbf{f}^D}} \mathbf{f}^D \frac{\partial \mathbf{f}^D}{\partial \tilde{\sigma}^j}, \quad J_{62} = J_{63} = 0, \quad J_{64} = -\frac{2(\lambda^j)^2}{3\sqrt{\frac{2}{3}(\lambda^j)^2 \mathbf{f}^D \cdot \mathbf{f}^D}} \mathbf{f}^D \frac{\partial \mathbf{f}^D}{\partial \epsilon_p^{Dj}}, \quad J_{65} = -\frac{2(\lambda^j)^2}{3\sqrt{\frac{2}{3}(\lambda^j)^2 \mathbf{f}^D \cdot \mathbf{f}^D}} \mathbf{f}^D \cdot \frac{\partial \mathbf{f}^D}{\partial \epsilon_p^j}, \quad J_{66} = \frac{1}{\Delta t} - \frac{2(\lambda^j)^2}{3\sqrt{\frac{2}{3}(\lambda^j)^2 \mathbf{f}^D \cdot \mathbf{f}^D}} \mathbf{f}^D \cdot \frac{\partial \mathbf{f}^D}{\partial \epsilon_{p \text{ eff}}^j}, \quad J_{67} = -\frac{2\lambda^j \mathbf{f}^D \cdot \mathbf{f}^D}{3\sqrt{\frac{2}{3}(\lambda^j)^2 \mathbf{f}^D \cdot \mathbf{f}^D}} \quad (\text{B.6})$$

Row 7:

$$J_{71} = \frac{\partial \zeta}{\partial F} \frac{\partial F}{\partial \tilde{\sigma}^j}, \quad J_{72} = J_{73} = 0, \quad J_{74} = \frac{\partial \zeta}{\partial F} \frac{\partial F}{\partial \epsilon_p^{Dj}}, \quad J_{75} = \frac{\partial \zeta}{\partial F} \frac{\partial F}{\partial \epsilon_p^j}, \quad J_{76} = \frac{\partial \zeta}{\partial F} \frac{\partial F}{\partial \epsilon_{p \text{ eff}}^j}, \quad J_{77} = -\eta_{\text{reg}} \quad (\text{B.7})$$

Appendix C. Linearization of the Minkley model

The viscosity function is linearised as

$$\frac{\partial \eta_M}{\partial \sigma_{\text{eff}}} = -\frac{\eta_{M0}}{\sigma_0} mn \left(\frac{\sigma_{\text{eff}}}{\sigma_0} \right)^{n-1} \frac{\coth[m(\sigma_{\text{eff}}/\sigma_0)^n]}{\sinh[m(\sigma_{\text{eff}}/\sigma_0)^n]} \quad (\text{C.1})$$

For the flow rule in Eq. (72) the (potential specific) derivatives are

$$\frac{\partial G_F}{\partial I_1} = \frac{1}{3} \sin \psi \quad (\text{C.2})$$

$$\frac{\partial G_F}{\partial J_2} = \begin{cases} \frac{1}{2\sqrt{J_2}} \left(\cos \theta - \frac{1}{\sqrt{3}} \sin \psi \sin \theta \right) & |\theta| < \theta_T \\ \frac{1}{2\sqrt{J_2}} (A' - B' \sin 3\theta) & |\theta| \geq \theta_T \end{cases} \quad (\text{C.3})$$

$$\frac{\partial G_F}{\partial \theta} = \begin{cases} -\sqrt{J_2} \left(\sin \theta + \frac{1}{\sqrt{3}} \sin \psi \cos \theta \right) & |\theta| < \theta_T \\ -\sqrt{J_2} 3B' \cos 3\theta & |\theta| \geq \theta_T \end{cases} \quad (\text{C.4})$$

and

$$\frac{\partial \theta}{\partial J_3} = \frac{\tan 3\theta}{3J_3} \quad (\text{C.5})$$

$$\frac{\partial \theta}{\partial J_2} = -\frac{\tan 3\theta}{2J_2} \quad (\text{C.6})$$

so that

$$\begin{aligned} \mathbf{f}^D &= \left(\frac{\partial G_F}{\partial J_2} + \frac{\partial G_F}{\partial \theta} \frac{\partial \theta}{\partial J_2} \right) \boldsymbol{\sigma}^D + \frac{\partial G_F}{\partial \theta} \frac{\partial \theta}{\partial J_3} J_3 (\boldsymbol{\sigma}^D)^{-1} : \mathcal{P}^D \quad \text{and} \\ \mathbf{f}^S &= \frac{\partial G_F}{\partial I_1} \mathbf{I} \quad \text{and} \quad f^S = 3 \frac{\partial G_F}{\partial I_1} \end{aligned} \quad (C.7)$$

Thus, the Jacobian's component relations can be closed as follows:

$$\frac{\partial \mathbf{f}^D}{\partial \tilde{\boldsymbol{\sigma}}^j} = G_M \frac{\partial \mathbf{f}^D}{\partial \boldsymbol{\sigma}^j}, \quad \frac{\partial \mathbf{f}^D}{\partial \epsilon_p^j} = \mathbf{0} \quad (C.8)$$

$$\frac{\partial \mathbf{f}^D}{\partial \epsilon_p^j} = \frac{\partial f^S}{\partial \tilde{\boldsymbol{\sigma}}^j} = \frac{\partial f^S}{\partial \epsilon_p^j} = \frac{\partial \mathbf{f}^D}{\partial \epsilon_p^j} = \frac{\partial F}{\partial \epsilon_p^j} = \mathbf{0} \quad (C.9)$$

$$\frac{\partial f^S}{\partial \epsilon_p^j} = \frac{\partial f^S}{\partial \epsilon_p^j} = \frac{\partial F}{\partial \epsilon_p^j} = \mathbf{0} \quad (C.10)$$

$$\frac{\partial F}{\partial \tilde{\boldsymbol{\sigma}}^j} = G_M \left[\frac{\partial F}{\partial I_1} \mathbf{I} + \left(\frac{\partial F}{\partial J_2} + \frac{\partial F}{\partial \theta} \frac{\partial \theta}{\partial J_2} \right) \boldsymbol{\sigma}^D + \frac{\partial F}{\partial \theta} \frac{\partial \theta}{\partial J_3} J_3 (\boldsymbol{\sigma}^D)^{-1} \mathcal{P}^D \right] \quad (C.11)$$

$$\frac{\partial F}{\partial \epsilon_p^j} = - \frac{\partial c}{\partial \epsilon_p^j} \cos \phi = -c_0 H \cos \phi \quad (C.12)$$

The linearization of \mathbf{f}^D follows:

$$\begin{aligned} \frac{\partial \mathbf{f}^D}{\partial \boldsymbol{\sigma}} &= \left(\frac{\partial G_F}{\partial J_2} + \frac{\partial G_F}{\partial \theta} \frac{\partial \theta}{\partial J_2} \right) \mathcal{P}^D + \frac{\partial G_F}{\partial \theta} \frac{\partial \theta}{\partial J_3} J_3 \mathcal{P}^D : \left((\boldsymbol{\sigma}^D)^{-1} \odot (\boldsymbol{\sigma}^D)^{-1} \right) : \mathcal{P}^D + \\ &+ \left(\frac{\partial^2 G_F}{\partial J_2^2} + \frac{\partial^2 G_F}{\partial \theta \partial J_2} \frac{\partial \theta}{\partial J_2} + \frac{\partial G_F}{\partial \theta} \frac{\partial^2 \theta}{\partial J_2^2} \right) \boldsymbol{\sigma}^D \otimes \boldsymbol{\sigma}^D + \\ &+ \left(\frac{\partial^2 G_F}{\partial J_2 \partial \theta} + \frac{\partial^2 G_F}{\partial \theta^2} \frac{\partial \theta}{\partial J_2} + \frac{\partial G_F}{\partial \theta} \frac{\partial^2 \theta}{\partial J_2 \partial \theta} \right) \\ &\times \left(\frac{\partial \theta}{\partial J_2} \boldsymbol{\sigma}^D \otimes \boldsymbol{\sigma}^D + \frac{\partial \theta}{\partial J_3} J_3 \boldsymbol{\sigma}^D \otimes [(\boldsymbol{\sigma}^D)^{-1} : \mathcal{P}^D] \right) + \\ &+ \frac{\partial^2 G_F}{\partial \theta \partial J_2} \frac{\partial \theta}{\partial J_3} J_3 [(\boldsymbol{\sigma}^D)^{-1} : \mathcal{P}^D] \otimes \boldsymbol{\sigma}^D \\ &+ \frac{\partial G_F}{\partial \theta} J_3 \left(\frac{\partial \theta}{\partial J_3} + \frac{\partial^2 \theta}{\partial J_3^2} J_3 \right) [(\boldsymbol{\sigma}^D)^{-1} : \mathcal{P}^D] \otimes [(\boldsymbol{\sigma}^D)^{-1} : \mathcal{P}^D] \\ &+ \left(\frac{\partial^2 G_F}{\partial \theta^2} \frac{\partial \theta}{\partial J_3} + \frac{\partial G_F}{\partial \theta} \frac{\partial^2 \theta}{\partial J_3 \partial \theta} \right) J_3 \\ &\left(\frac{\partial \theta}{\partial J_2} [(\boldsymbol{\sigma}^D)^{-1} : \mathcal{P}^D] \otimes \boldsymbol{\sigma}^D + \frac{\partial \theta}{\partial J_3} J_3 [(\boldsymbol{\sigma}^D)^{-1} : \mathcal{P}^D] \otimes [(\boldsymbol{\sigma}^D)^{-1} : \mathcal{P}^D] \right) \end{aligned} \quad (C.13)$$

with

$$\frac{\partial^2 G_F}{\partial J_2^2} = \begin{cases} -\frac{1}{4\sqrt{J_2}} \left(\cos \theta - \frac{1}{\sqrt{3}} \sin \psi \sin \theta \right) & |\theta| < \theta_T \\ -\frac{1}{4\sqrt{J_2}} (A' - B' \sin 3\theta) & |\theta| \geq \theta_T \end{cases} \quad (C.14)$$

$$\frac{\partial^2 G_F}{\partial \theta \partial J_2} = \frac{\partial^2 G_F}{\partial J_2 \partial \theta} = \begin{cases} -\frac{1}{2\sqrt{J_2}} \left(\sin \theta + \frac{1}{\sqrt{3}} \sin \psi \cos \theta \right) & |\theta| < \theta_T \\ -\frac{1}{2\sqrt{J_2}} 3B' \cos 3\theta & |\theta| \geq \theta_T \end{cases} \quad (C.15)$$

$$\frac{\partial^2 G_F}{\partial \theta^2} = \begin{cases} -\sqrt{J_2} \left(\cos \theta - \frac{1}{\sqrt{3}} \sin \psi \sin \theta \right) & |\theta| < \theta_T \\ \sqrt{J_2} 9B' \sin 3\theta & |\theta| \geq \theta_T \end{cases} \quad (C.16)$$

$$\frac{\partial^2 \theta}{\partial J_2^2} = \frac{\tan 3\theta}{2J_2^2} \quad (C.17)$$

$$\frac{\partial^2 \theta}{\partial J_2 \partial \theta} = -\frac{3}{2J_2} \sec^2 3\theta = -\frac{3}{2J_2 \cos^2 3\theta} \quad (C.18)$$

$$\frac{\partial^2 \theta}{\partial J_3 \partial \theta} = \frac{1}{J_3} \sec^2 3\theta = \frac{1}{J_3 \cos^2 3\theta} \quad (C.19)$$

$$\frac{\partial^2 \theta}{\partial J_3^2} = -\frac{\tan 3\theta}{3J_3^2} \quad (C.20)$$

References

- [1] Minkley W, Mühlbauer J, Lüdeling C. Dimensioning principles in potash and salt mining to achieve stability and integrity. In: 49th US rock mechanics/geomechanics symposium. American Rock Mechanics Association; 2015.
- [2] Minkley W, Knauth M, Brückner D. Discontinuum-mechanical behaviour of salt rocks and the practical relevance for the integrity of salinar barriers. In: 47th US rock mechanics/geomechanics symposium. American Rock Mechanics Association; 2013.
- [3] Minkley W, Knauth M, Fabig T, Farag N. Stability and integrity of salt caverns under consideration of hydro-mechanical loading. In: Mechanical behaviour of salt VIII. CRC Press; 2015. p. 217–27. <http://dx.doi.org/10.1201/b18393-29>.
- [4] Pudewills A, Müller-Hoeppel N, Papp R. Thermal and thermomechanical analyses for disposal in drifts of a repository in rock salt. Nucl Technol 1995;112(1):79–88.
- [5] Hunsche U, Schulze O. Das Kriechverhalten von Steinsalz. Kali Steinsalz 1994;11(8/9):238–55.
- [6] Harris AF, McDermott C, Kolditz O, Haszeldine R. Modelling groundwater flow changes due to thermal effects of radioactive waste disposal at a hypothetical repository site near Sellafield, UK. Environ Earth Sci 2015;74(2):1589–602.
- [7] Li M, Zhang H, Xing W, Hou Z, Were P. Study of the relationship between surface subsidence and internal pressure in salt caverns. Environ Earth Sci 2015;73(11):6899–910.
- [8] Xing W, Zhao J, Hou Z, Were P, Li M, Wang G. Horizontal natural gas caverns in thin-bedded rock salt formations. Environ Earth Sci 2015;73(11):6973–85.
- [9] Safaei H, Keith DW, Hugo RJ. Compressed air energy storage (CAES) with compressors distributed at heat loads to enable waste heat utilization. Appl Energy 2013;103(0):165–79. <http://dx.doi.org/10.1016/j.apenergy.2012.09.027>. <<http://www.sciencedirect.com/science/article/pii/S030626191200668X>>.
- [10] Greenblatt JB, Succar S, Denkenberger DC, Williams RH, Soclow RH. Baseload wind energy: modeling the competition between gas turbines and compressed air energy storage for supplemental generation. Energy Policy 2007;35(3):1474–92. <<http://www.sciencedirect.com/science/article/pii/S0301421506001509>>.
- [11] Ibrahim H, Ilinca A, Perron J. Energy storage systems – characteristics and comparisons. Renew Sust Energy Rev 2008;12(5):1221–50. <<http://www.sciencedirect.com/science/article/pii/S1364032107000238>>.
- [12] Lund H, Salgi G. The role of compressed air energy storage (CAES) in future sustainable energy systems. Energy Convers Manage 2009;50(5):1172–9. <<http://www.sciencedirect.com/science/article/pii/S0196890409000429>>.
- [13] Lund H, Salgi G, Elmegaard B, Andersen AN. Optimal operation strategies of compressed air energy storage (CAES) on electricity spot markets with fluctuating prices. Appl Therm Eng 2009;29(5):799–806. <<http://www.sciencedirect.com/science/article/pii/S1359431108002469>>.
- [14] Ma H, Yang C, Li Y, Shi X, Liu J, Wang T. Stability evaluation of the underground gas storage in rock salts based on new partitions of the surrounding rock. Environ Earth Sci 2015;73(11):6911–25.
- [15] Lux KH, Rokahr R. Laboratory investigations and theoretical statements as a basis for the design of cavern in rock salt formation. In: Proceedings of the 1st conference on the mechanical behavior of salt. p. 169–79.
- [16] Lux K-H. Gebirgsmechanischer Entwurf und Felderfahrungen im Salzkavernenbau: ein Beitrag zur Entwicklung von Prognosemodellen für den Hohlraumbau im duktilen Salzgebirge. Stuttgart: Ferdinand Enke Verlag; 1984.
- [17] Cristescu N. Irreversible dilatancy or compressibility of viscoplastic rock-like materials and some applications. Int J Plasticity 1985;1(3):189–204.
- [18] Pudewills A, Droste J. Numerical modeling of the thermomechanical behavior of a large-scale underground experiment. Comput Struct 2003;81(8):911–8.
- [19] Pudewills A. Numerical modelling of the long-term evolution of EDZ: development of material models, implementation in finite-element codes, and validation. Wissenschaftliche Berichte FZKA; 7185.
- [20] Cristescu N. A procedure to determine nonassociated constitutive equations for geomaterials. Int J Plasticity 1994;10(2):103–31.
- [21] Cristescu ND, Hunsche U. Time effects in rock mechanics. New York: Wiley; 1998.
- [22] Heusermann S, Lux K-H, Rokahr R. Entwicklung mathematisch-mechanischer Modelle zur Beschreibung des Stoffverhaltens von Salzgestein in Abhängigkeit von der Zeit und der Temperatur auf der Grundlage von Laborversuchen mit

- begleitenden kontinuumsmechanischen Berechnungen nach der Methode der finiten Elemente. Fachinformationszentrum Energie, Physik, Mathematik Karlsruhe; 1983.
- [23] Desai C, Zhang D. Viscoplastic model for geologic materials with generalized flow rule. *Int J Numer Anal Methods Geomech* 1987;11(6):603–20.
 - [24] Jin J, Cristescu N. An elastic/viscoplastic model for transient creep of rock salt. *Int J Plasticity* 1998;14(1):85–107.
 - [25] Chan K, Brodsky N, Fossum A, Bodner S, Munson D. Damage-induced nonassociated inelastic flow in rock salt. *Int J Plasticity* 1994;10(6):623–42.
 - [26] Minkley W. Gebirgsmechanische Beschreibung von Entfestigung und Sprödbucherscheinungen im Carnallitit. Shaker; 2004.
 - [27] Minkley W, Menzel W, Konietzky H, te Kamp L. A visco-elasto-plastic softening model and its application for solving static and dynamic stability problems in potash mining. In: DB. et al. editors. *FLAC and numerical modeling in geomechanics – 2001* (proceedings of the 2nd international FLAC conference, Lyon, France); 2001. p. 27.
 - [28] Minkley W, Mühlbauer J. Constitutive models to describe the mechanical behavior of salt rocks and the imbedded weakness planes. In: Wallner M, Lux K, Minkley W, Hardy H, editors. *The mechanical behaviour of salt – understanding of THMC processes in salt: 6th conference (SaltMech6)*, Hannover, Germany. p. 119–27.
 - [29] Hampel A, Günther R, Salzer K, Minkley W, Pudewills A, Leuger B, et al. BMBF-Verbundprojekt: Vergleich aktueller Stoffgesetze und Vorgehensweisen anhand von 3D-Modellberechnungen zum mechanischen Langzeitverhalten eines realen Untertagebauwerks im Steinsalz. Tech. rep.; 2010.
 - [30] Heusermann S, Rolfs O, Schmidt U. Nonlinear finite-element analysis of solution mined storage caverns in rock salt using the LUBBY2 constitutive model. *Comput Struct* 2003;81(811):629–38. [http://dx.doi.org/10.1016/S0045-7949\(02\)00415-7](http://dx.doi.org/10.1016/S0045-7949(02)00415-7). kJ Bathe 60th Anniversary Issue <<http://www.sciencedirect.com/science/article/pii/S0045794902004157>>.
 - [31] Wang G, Guo K, Christianson M, Konietzky H. Deformation characteristics of rock salt with mudstone interbeds surrounding gas and oil storage cavern. *Int J Rock Mech Mining Sci* 2011;48(6):871–7. URL <http://www.sciencedirect.com/science/article/pii/S1365160911001134>.
 - [32] Nazary Moghadam S, Mirzabozorg H, Noorzad A. Modeling time-dependent behavior of gas caverns in rock salt considering creep, dilatancy and failure. *Tunn Undergr Space Technol* 2013;33:171–85.
 - [33] Pfeifle T, Brodsky N, Munson D. Experimental determination of the relationship between permeability and microfracture-induced damage in bedded salt. *Int J Rock Mech Mining Sci* 1998;35(4):593–4.
 - [34] Pudewills A. Modelling of the hydro-mechanical processes around excavations in rock salt. In: *Proc of EUROCK*.
 - [35] Le TM, Fatahi B, Khabbaz H. Numerical optimisation to obtain elastic viscoplastic model parameters for soft clay. *Int J Plasticity* 2015;65:1–21. <http://dx.doi.org/10.1016/j.iplas.2014.08.008>. <<http://www.sciencedirect.com/science/article/pii/S0749641914001624>>.
 - [36] Ma J, Zhao G, Khalili N. A fully coupled flow deformation model for elastoplastic damage analysis in saturated fractured porous media. *Int J Plasticity* 2016;76:29–50. <http://dx.doi.org/10.1016/j.iplas.2015.07.011>. <<http://www.sciencedirect.com/science/article/pii/S0749641915001370>>.
 - [37] Pudewills A, Krauss M. Implementation of a viscoplastic model for crushed salt in the adina program. *Comput Struct* 1999;72(1):293–9.
 - [38] Kolditz O, Bauer S, Bilke L, Böttcher N, Delfs J, Fischer T, et al. OpenGeoSys: an open-source initiative for numerical simulation of thermo-hydro-mechanical/chemical (THM/C) processes in porous media. *Environ Earth Sci* 2012;67(2):589–99.
 - [39] Cordts D, Kollmann FG. An implicit time integration scheme for inelastic constitutive equations with internal state variables. *Int J Numer Methods Eng* 1986;23(4):533–54.
 - [40] Kobayashi M, Mukai M, Takahashi H, Ohno N, Kawakami T, Ishikawa T. Implicit integration and consistent tangent modulus of a time-dependent non-unified constitutive model. *Int J Numer Methods Eng* 2003;58(10):1523–43.
 - [41] Kouhia R, Marjamäki P, Kivilahti J. On the implicit integration of rate-dependent inelastic constitutive models. *Int J Numer Methods Eng* 2005;62(13):1832–56.
 - [42] Larsson R, Runesson K. Implicit integration and consistent linearization for yield criteria of the Mohr–Coulomb type. *Mech Cohesive-Frict Mater* 1996;1(4):367–83.
 - [43] Bucher A, Görke U-J, Kreißig R. A material model for finite elasto-plastic deformations considering a substructure. *Int J Plasticity* 2004;20(4):619–42.
 - [44] Lush A, Weber G, Anand L. An implicit time-integration procedure for a set of internal variable constitutive equations for isotropic elasto-viscoplasticity. *Int J Plasticity* 1989;5(5):521–49.
 - [45] Zienkiewicz OC, Taylor RL, Zhu JZ. *The finite element method set*. 6th ed. Oxford: Elsevier Butterworth-Heinemann; 2006. <<http://www.worldcat.org/oclc/636432933>>.
 - [46] Simo JC, Hughes TJR. Objective integration algorithms for rate formulations of elastoplasticity. In: *Computational inelasticity. Interdisciplinary applied mathematics*, vol. 7. New York: Springer; 1998. p. 276–99. <http://dx.doi.org/10.1007/0-387-22763-6_8>.
 - [47] Andrade F, Pires FA, de Sa JC. Consistent tangent operators for implicit non-local models of integral type. *Comput Struct* 2014;141:59–73.
 - [48] Safaei M, Yoon JW, Waele WD. Study on the definition of equivalent plastic strain under non-associated flow rule for finite element formulation. *Int J Plasticity* 2014;58:219–38. <http://dx.doi.org/10.1016/j.iplas.2013.09.010>. in Honor of Kwansoo Chung <<http://www.sciencedirect.com/science/article/pii/S0749641913001903>>.
 - [49] Brepolis T, Vladimirov IN, Reese S. Numerical comparison of isotropic hypo- and hyperelastic-based plasticity models with application to industrial forming processes. *Int J Plasticity* 2014;63:18–48. <http://dx.doi.org/10.1016/j.iplas.2014.06.003>. deformation Tensors in Material Modeling in Honor of Prof. Otto T. Bruhns <<http://www.sciencedirect.com/science/article/pii/S0749641914001259>>.
 - [50] Zhu Y, Kang G, Kan Q, Bruhns OT. Logarithmic stress rate based constitutive model for cyclic loading in finite plasticity. *Int J Plasticity* 2014;54:34–55. <http://dx.doi.org/10.1016/j.iplas.2013.08.004>. <<http://www.sciencedirect.com/science/article/pii/S0749641913001599>>.
 - [51] Haouala S, Doghri I. Modeling and algorithms for two-scale time homogenization of viscoelastic-viscoplastic solids under large numbers of cycles. *Int J Plasticity* 2015;70:98–125. <http://dx.doi.org/10.1016/j.iplas.2015.03.005>. <<http://www.sciencedirect.com/science/article/pii/S0749641915000480>>.
 - [52] Mengoni M, Ponthot J. A generic anisotropic continuum damage model integration scheme adaptable to both ductile damage and biological damage-like situations. *Int J Plasticity* 2015;66:46–70. <http://dx.doi.org/10.1016/j.iplas.2014.04.005>. plasticity of Textured Polycrystals In Honor of Prof. Paul Van Houtte <<http://www.sciencedirect.com/science/article/pii/S0749641914000874>>.
 - [53] Bauer S, Beyer C, Dethlefsen F, Dietrich P, Duttman R, Ebert M, et al. Impacts of the use of the geological subsurface for energy storage: an investigation concept. *Environ Earth Sci* 2013;70(8):3935–43.
 - [54] Perzyna P. Fundamental problems in viscoplasticity. *Adv Appl Mech* 1966;9:243.
 - [55] Heeres OM, Suiker AS, de Borst R. A comparison between the perzyna viscoplastic model and the consistency viscoplastic model. *Eur J Mech – A/ Solids* 2002;21(1):1–12.
 - [56] Nagel T, Görke U-J, Moerman KM, Kolditz O. On advantages of the kelvin mapping in finite element implementations of deformation processes. *Environ Earth Sci* 2016;75(11):1–11. <http://dx.doi.org/10.1007/s12665-016-5429-4>. <<http://dx.doi.org/10.1007/s12665-016-5429-4>>.
 - [57] Bucher A, Görke U-J, Kreißig R. Development of a generalized material interface for the simulation of finite elasto-plastic deformations. *Int J Solids Struct* 2001;38(52):9423–36.
 - [58] Lewis RW, Schrefler BA. *The finite element method in the static and dynamic deformation and consolidation of porous media*. 2nd ed. Chichester [u.a.]: Wiley; 1998. <<http://www.loc.gov/catdir/toc/onix04/98012080.html>>.
 - [59] Heusermann S, Vogel P, Eickemeier R, Nipp H. Thermomechanical modelling of the gorleben exploration site to analyse the integrity of the salt barrier. *Artif Neural Networks Biol Environ Anal* 2011:239.
 - [60] Fahland S, Heusermann S. Measurement and calculation of rock stress in the morsleben repository. In: *Proceedings of the seventh international. Conference on the mechanical behavior of salt (SaltMech7)*, Paris, 16–19 April 2012. p. 193–200.
 - [61] Cyr ED, Mohammadi M, Mishra RK, Inal K. A three dimensional (3d) thermo-elasto-viscoplastic constitutive model for {FCC} polycrystals. *Int J Plasticity* 2015;70:166–90. <http://dx.doi.org/10.1016/j.iplas.2015.04.001>. <<http://www.sciencedirect.com/science/article/pii/S0749641915000571>>.
 - [62] Haupt P. *Continuum mechanics and theory of materials*. Springer; 2002.
 - [63] Wang W, Sluys L, De Borst R. Viscoplasticity for instabilities due to strain softening and strain-rate softening. *Int J Numer Methods Eng* 1997;40(20):3839–64.
 - [64] Nayak G, Zienkiewicz O. Elasto-plastic stress analysis. A generalization for various constitutive relations including strain softening. *Int J Numer Methods Eng* 1972;5(1):113–35. <<http://onlinelibrary.wiley.com/doi/10.1002/nme.1620050111/abstract>>.
 - [65] de Borst R, Heeres OM. A unified approach to the implicit integration of standard, non-standard and viscous plasticity models. *Int J Numer Anal Methods Geomech* 2002;26(11):1059–70.
 - [66] Chaboche J. A review of some plasticity and viscoplasticity constitutive theories. *Int J Plasticity* 2008;24(10):1642–93.
 - [67] Niazi M, Wisselink H, Meinders T. Viscoplastic regularization of local damage models: revisited. *Comput Mech* 2013;51(2):203–16.
 - [68] McAuliffe C, Waisman H. On the importance of nonlinear elastic effects in shear band modeling. *Int J Plasticity* 2015;71:10–31. <http://dx.doi.org/10.1016/j.iplas.2015.04.004>. <<http://www.sciencedirect.com/science/article/pii/S0749641915000601>>.
 - [69] Sloan S, Booker J. Removal of singularities in tresca and mohr–coulomb yield functions. *Commun Appl Numer Methods* 1986;2(2):173–9. <<http://onlinelibrary.wiley.com/doi/10.1002/cnm.1630020208/abstract>>.
 - [70] Borja RI, Sama KM, Sanz PF. On the numerical integration of three-invariant elastoplastic constitutive models. *Comput Methods Appl Mech Eng* 2003;192(9):1227–58. <<http://www.sciencedirect.com/science/article/pii/S0045782502006205>>.
 - [71] Carlson DE, Hoger A. The derivative of a tensor-valued function of a tensor. *Quart Appl Math* 1986;44(3):409–23.
 - [72] Friswell M. The derivatives of repeated eigenvalues and their associated eigenvectors. *J Vib Acoust* 1996;118(3):390–7.
 - [73] Arroyo M, Belytschko T. Finite element methods for the non-linear mechanics of crystalline sheets and nanotubes. *Int J Numer Methods Eng* 2004;59(3):419–56.

- [74] Zienkiewicz O, Corneau I. Visco-plasticity – plasticity and creep in elastic solids – a unified numerical solution approach. *Int J Numer Methods Eng* 1974;8(4):821–45. <<http://onlinelibrary.wiley.com/doi/10.1002/nme.1620080411/abstract>>.
- [75] Sriapai T, Walsri C, Fuenkajorn K. Effect of temperature on compressive and tensile strengths of salt. *ScienceAsia* 2012;38(2):166–74.
- [76] Du C, Yang C, Yao Y, Li Z, Chen J. Mechanical behaviour of deep rock salt under the operational conditions of gas storage. *Int J Earth Sci Eng* 2012;5(6):1670–6.
- [77] Senseny P, Lindberg H, Schwer L. Elastic–plastic response of a circular hole to repeated loading. *Int J Numer Anal Methods Geomech* 1989;13(5):459–76.
- [78] Wang W, Kosakowski G, Kolditz O. A parallel finite element scheme for thermo-hydro-mechanical (THM) coupled problems in porous media. *Comput Geosci* 2009;35(8):1631–41.
- [79] Wang W, Kolditz O, Nagel T. Parallel finite element modelling of multi-physical processes in thermochemical energy storage devices. *Appl Energy* 2016.